Dampening effect of global flows on Rayleigh-Taylor instabilities: Implications for deep-mantle plume vis-à-vis hotspot distributions

Arnab Roy, Dip Ghosh and Nibir Mandal

Department of Geological Sciences, Jadavpur University
Kolkata 700032, India

This manuscript has been submitted for publication in Geophysical Journal International. Please note that the manuscript has undergone two rounds of peer-review process and is presently under review. Subsequent versions of this manuscript may have slightly different content. If accepted, the final version of this manuscript will be available via a link on this webpage. Please feel free to contact any of the authors if you have questions or feedback.

Dampening effect of global flows on Rayleigh-Taylor instabilities: Implications for deep-mantle plumes vis-à-vis hotspot distributions

Journal:	*Geophysical Journal International*
Manuscript ID	GJI-S-23-0401.R1
Manuscript Type:	Research Paper
Date Submitted by the Author:	n/a
Complete List of Authors:	Roy, Arnab; Jadavpur University Faculty of Science, Geological Sciences Ghosh, Dip; Jadavpur University, Geological Sciences Mandal, Nibir; Jadavpur University, Department of Geological Sciences
Additional Keywords:	
Keywords:	Dynamics: convection currents, and mantle plumes < TECTONOPHYSICS, Instability analysis < GEOPHYSICAL METHODS, Numerical modelling < GEOPHYSICAL METHODS, Hotspots < TECTONOPHYSICS, Mantle processes < TECTONOPHYSICS

Summary

It is a well-accepted hypothesis that deep-mantle primary plumes originate from a buoyant source layer at the core-mantle boundary (CMB), where Rayleigh–Taylor (RT) instabilities play a key role in the plume initiation process. Previous studies have characterized their growth rates mainly in terms of the density, viscosity and layer-thickness ratios between the denser overburden and the source layer. The RT instabilities, however, develop in the presence of global flows in the overlying mantle, which can act as an additional factor in the plume mechanics. Combining 2D computational fluid dynamic (CFD) model simulations and a linear stability analysis, this article explores the influence of a horizontal global mantle flow in the instability dynamics. Both the CFD simulation results and analytical solutions reveal that the global flow is a dampening factor in reducing the instability growth rate. At a threshold value of the normalized global flow velocity, short as well as long wavelength instabilities are completely suppressed, allowing the entire system to advect in the horizontal direction. Using a series of real-scale numerical simulations this article also investigates the growth rate as a function of the density contrast, expressed in Atwood number $A_T = (\rho_1 - \rho_2)/(\rho_1 + \rho_2)$, and the viscosity ratio $\mu^* = \mu_1/\mu_2$, where ρ_1, μ_1 and ρ_2, μ_2 are densities and viscosities of the overburden mantle and source-layer, respectively. It is found that increase in either A_T or μ^* promotes the growth rate of a plume. In addition, the stability analysis predicts a nonlinearly increasing RT instability wavelength with increasing global flow velocity, implying that the resulting plumes widen their spacing preferentially in the flow direction of kinematically active mantle regions. The theory accounts for additional physical parameters: source-layer viscosity and thickness in the analysis of the dominant wavelengths and their corresponding growth rates. The article finally discusses the problem of unusually large inter-hotspot spacing, providing a new conceptual framework for the origin of sporadically distributed hotspots of deep-mantle sources.

Keywords: Hotspots, Mantle processes, Dynamics: convection currents, and mantle plumes, Numerical modelling, Instability analysis

1. Introduction

Rayleigh-Taylor (RT) instability, primarily driven by gravitational forces in inverted density stratification, i.e., a heavy fluid resting upon a relatively light fluid, governs a wide range of atmospheric and oceanic processes, e.g., global air circulation, cloud formation, oceanic currents as well as many interstellar, and planetary phenomena, e.g., supernova explosion and silicate-metal segregation. Lord Rayleigh and G.I. Taylor first predicted the RT instability growth rate from a linear stability analysis, considering the effects of inertial and body forces between two immiscible inviscid fluids (Rayleigh 1882; Taylor 1950). Since then, the RT theory continued to proliferate in diverse directions (Zhou 2017a; b; Zhou *et al.* 2019, 2021) with the addition of increasing physical variables to the theoretical treatment, such as, surface tension (Pullin 1982; Mikaelian 1996), density gradient (Munro 1988; Song *et al.* 2021), diffusion (Masse 2007), temperature gradient and mass transfer (Gerashchenko & Livescu 2016), effect of rotation (Baldwin *et al.* 2015) and magnetic field (Zrnić & Hendricks 2003). A category of these variables (density gradient, temperature gradient, mass transfer, and diffusion) facilitates the growth of instabilities, whereas the others (surface tension, magnetic field, and rotational forces), in contrast, act as dampening agencies. A complete theory thus demands an account of both the driving and dampening factors to predict the dynamics of gravitational instabilities in natural systems as well as practical applications. The RT instability mechanics has been also extensively applied in solid earth geophysics to conceptualize many important geodynamic processes (Turcotte & Schubert 2002), such as salt dome formation in sedimentary basins (Ramberg 1968a; b, 1972; Miller & Behn 2012; Louis-Napoleon *et al.* 2022), magma transport (Whitehead 1986; Wilcock & Whitehead 1991), intraplate orogenic collapse (Neil & Houseman 1999; Louis-Napoléon *et al.* 2020), downwelling at the lithospheric base (Conrad & Molnar 1997; Houseman & Molnar 1997), silicate mantle-metallic core segregation in the Earth (Ida *et al.* 1987; Mondal & Korenaga 2018). The success of these applications has greatly widened the research scope of mantle dynamics in the light of gravitational instabilities.

Plume formation is recognized as the most effective geodynamic process to drive focused upwelling in Earth's mantle, and it is a well-accepted hypothesis that they originate mostly from RT instabilities in the thermal boundary layer (TBL) at the core-mantle boundary (CMB) (Morgan 1972; Nolet et al. 2007; Burke et al. 2008; Styles et al. 2011) and other regions at relatively shallower depths, such as melt-rich zones above sinking slabs in subduction zones (Gerya & Yuen 2003; Ghosh, Maiti, Mandal, *et al.* 2020) and transition zones (Brunet & Yuen 2000; Kumagai *et al.* 2007). Plumes initiated by instabilities in the TBL ascend under buoyancy forces of their large heads (~500 to >1000 km in diameter), which trail into narrow tails (~100 to 200 km in diameter). Scaled laboratory experiments and numerical simulations have provided significant insights into their ascent behaviour (Whitehead & Luther 1975; Olson & Singer 1985; Bercovici & Kelly 1997; Lowman et al. 2004; Ballmer et al. 2011). Jellinek et al. (2002) demonstrated from analogue experiments that, under a thermal equilibrium condition the dynamic topography in the TBL formed as a consequence of RT instabilities determines the relative spacing of upwelling zones. Similar laboratory experiments showed entrainment of surrounding materials by the bulbous plume heads during their ascent (van Keken et al., 1997). Several experimental studies have reported the transient behaviour of thermal plumes (Davaille & Vatteville 2005) and their geometrical asymmetry as a function of source-layer inclination (Dutta *et al.* 2016). On the other direction, a number of CFD models, both 2D and 3D, have shown the formation of thermal plumes from the D" layer in Earth's mantle (Montague & Kellogg 2000; Jones *et al.* 2016; Li & Zhong 2017; Frazer & Korenaga 2022). This approach has set a new ground for the plume research to deal with complex ascent dynamics resulting from the interplay of multiple physical factors, e.g., viscoplastic rheology in the lower mantle (Davaille et al. 2018) and thermo-mechanical heterogeneities in TBL (Heyn *et al.* 2018).

To tackle the problem of mantle plume generation, a line of earlier experimental, theoretical and numerical studies, as discussed above investigated the mechanics of plume formation within a framework of RT instability theory applicable for initially rest stratified fluid systems (Jellinek & Manga 2004). The overlying heavy fluid chosen to represent the mantle is set to flow entirely under the destabilizing gravity effect of inverted density stratification. However, the assumption of an initially rest kinematic state is hardly valid in Earth's interior because the mantle regions are inherently under the influence of large-scale global flows that originate from various geodynamic processes (Fig. 1), such as down-going slab movement, lithospheric plate motions, global convection and mantle winds (Bekaert *et al.* 2021). Plumes, irrespective of their thermal or thermo-chemical origin, therefore, evolve through kinematic interactions with the ambient mantle flows. Some of the recent studies showed their complex development under the influence of mantle convection (Li & Zhong 2017; Negredo *et al.* 2022; Bredow *et al.* 2023). However, how horizontal global mantle flows can modulate their ascent behaviour is still debated. For example, Korenaga (2005) hypothesized that mantle plumes remain fixed in their spatial positions despite an active background flow in the mantle, as observed from seismic images of deep-mantle plumes. Another school holds a completely opposite view, claiming that deep-sourced plumes undergo horizontal deflections under the influence of global flows (e.g., Steinberger & O'Connell 1998), which are also demonstrated from laboratory experiments (Griffiths & Richards 1989; Mark A. Richards & Griffiths 1989; Kerr & Mériaux 2004; Kerr *et al.* 2008). Despite a significant progress in the plume study, it is yet to address the most critical questions: 1) in what way does a background flow influence the onset of RT instabilities for plume formation;

2) does the flow facilitates or dampens the instability growth? These unresolved issues constitute the central theme of our present article.

Using a 2D finite element particle-in-cell numerical method we performed computational fluid dynamics (CFD) simulation experiments to investigate the problem of RT instability growth at the CMB in mantle subjected to a global horizontal flow. The CFD simulations are utilized to explore the existence of a threshold global velocity at which the instability can be completely suppressed, allowing no plume to grow from the buoyant basal layer. We also develop a linear stability analysis to derive a dispersion relation of RT instabilities as a function of layer-parallel flow in the overlying mantle and support our findings from the simulations. Based on the numerical model findings and analytical solution, this study finally provides a possible explanation for the sporadic spatial distribution of hotspots on Earth's surface.

2. CFD Modelling

2.1. Model Approach

We model mantle plumes initiated by Rayleigh Taylor Instability (RTI) in a 1×2.69 rectangular domain (Fig. 2), considering the lower-mantle thickness (2230 km) as the reference length scale (L_o) to normalize the model length dimensions. The model consists of a thin, low-density layer with thickness h_2 = 0.045 at its base, overlain by a denser layer with much greater thickness h_1 = 0.955. The thin layer at the model base is chosen to mechanically replicate a buoyant boundary layer above the Core-Mantle boundary (CMB), described as *source layer* in the foregoing discussion. The source layer faces gravity driven RTI due to density inversion, forming plumes in course of the instability evolution. We develop our CFD modelling in the framework of incompressible Stokes flow mechanics, using the mass and momentum conservation equations:

$$\nabla . \boldsymbol{u} = 0, \qquad (1)$$

$$-\nabla P + \nabla . \left(\mu_i (\nabla \boldsymbol{u} + \nabla^T \boldsymbol{u})\right) + \rho_i \boldsymbol{g} = \boldsymbol{0} \qquad (2)$$

where, $\boldsymbol{u}$ is the velocity, μ_i is the viscosity of the medium *i*, *P* is the total pressure, $\boldsymbol{g}$ is the acceleration due to gravity, and ρ_i is the density of the medium *i*. Earlier studies have provided different estimates for the lower-mantle viscosity, e.g., ~10^{22} Pa s from geoid anomalies (Richards & Hager 1984), slightly higher than 10^{21} Pa s from postglacial rebound (Cathles 1975; Spada *et al.* 1991). Numerical modelling, on the other hand, yields an estimate of ~$3\text{x}10^{22}$ Pa s from the slab sinking rates (Čížková *et al.* 2012). Considering these estimates, we set the reference viscosity μ_0 at 10^{22} Pa s to normalize the model-layer viscosities. The overburden layer is assigned a normalized viscosity $\mu_1 = 1$, which is held constant to represent the average lower-mantle viscosity and simplify the model setup with an aim to find additional effects of global horizontal flows on the dynamics of plume formation in Earth's mantle. We, however, varied the source-layer viscosity μ_2 in the range 0.0001 - 0.1 (Nakada *et al.* 2012) to account for the mechanical effects of various lateral thermal and chemical heterogeneities at the base of lower mantle reported by several authors (Davies *et al.* 2012; Farnetani *et al.* 2018). In our model we introduce an initial perturbation $F(y)$ at the interface between the two fluid layers as,

$$F(y) = h_2 + \Delta A(\cos(kx)) \qquad (3)$$

where $\Delta A = 8.97 \times 10^{-6}, k = \frac{2\pi}{\lambda}$, and $\lambda = 0.54$.

To describe the simulation results, we express the source-layer viscosity μ_2 relative to the overlying mantle viscosity $\mu_1$as, $\mu^* = \frac{\mu_1}{\mu_2}$. Similarly, the density contrast (buoyancy factor) of the fluids is non-dimensionalized in terms of Atwood number (A_T), expressed by:

$$A_T = \frac{\rho_1 - \rho_2}{\rho_1 + \rho_2} \qquad (4)$$

where ρ_1 and ρ_2 are the densities of heavier overburden and lighter source-layer, respectively. All the notations and their corresponding physical variables are summarised in Table 1. A_T is varied in the range 0.01 to 0.04 (Nipin & Tomar 2015). We also normalize the RTI wavelength (λ_c) with source-layer thickness (h_2) as $\lambda^* = \frac{\lambda_c}{h_2}$.

We impose a kinematic boundary condition at the upper model boundary to introduce a global flow in the model mantle, which is the prime concern of our present study (Fig. 2). The bottom wall is assigned a no-slip boundary condition (choice of bottom boundary condition elaborated in Supplementary S1), whereas the two side walls are subjected to periodic boundary condition. We use the open-source finite element code UNDERWORLD2 (http://www.underworldcode.org/) to solve the mass and momentum conservation equations (Eq. 1 and 2) for the CFD simulations. This code works within a continuum mechanics approximation, and has been extensively used to deal with a range of geological and geophysical problems (Mansour *et al.* 2020). As explained in Moresi et al. (2007) and Mansour et al. (2020), the code discretizes the geometrical domain into a standard Eulerian finite element mesh and the domain is coupled with the particle-in-cell approach (Evans *et al.* 1957). In this numerical approach each fluid space is discretised into Lagrangian material points, ensuring the accurate tracking of material interfaces and history information using particle swarms = 20971520, over the entire simulation run. The mass and momentum conservation equations are solved to find the pressure and velocity conditions within the model domain. Physical parameters, such as density and viscosity associated with Earth's interior are coupled to these equations through particle indexing (Roy et al. 2021; Roy et al. 2022). The numerical model domain is discretized into 1024 x 512 rectangular elements. Mesh resolution tests were performed to assess the mesh resolution effects on simulation results (details in Supplementary S2). To verify the applicability of the UNDERWORLD2 code in solving the problems of RT instability in a mechanical setting with large viscosity contrasts, we have carried out the Rayleigh–Taylor instability and falling block benchmark experiments and compared the results with the solutions available in previous studies (van Keken et al. 1997; Thieulot 2011, 2014; Gerya 2019). The details of these benchmark tests are provided separately in Appendix A.

2.2. Model Results

2.2.1. Dampening effects of horizontal global flows

We systematically increased the top model-boundary velocity (U_o) to evaluate the effect of global flows on the growth rates of instabilities in the source layer, estimated from the vertical ascent-velocity component of instability-driven domes. Following Ramberg's (1968) theoretical formulation, U_o is normalised with the absolute value of instantaneous ascent velocity v_y ,

$$\frac{v_y}{\Delta A_{time}} = -K\frac{\rho_1 - \rho_2}{2\mu_2} h_2 g, \quad (5)$$

where K is a non-dimensional constant that depends on the viscosity and the wavelength of the system under consideration (details provided in Supplementary S3). ΔA_{time} denotes the amplitude of interface perturbations calculated from numerical simulations at the time (t ~ 0.052) the instability starts to grow exponentially. This ascent velocity value (0.833 cm/year) is set as the reference velocity v_0 value for all the simulations. The normalised boundary velocity, $U^* = \frac{U_0}{|v_0|}$ was varied in the range 0 to ~36, keeping A_T (= 0.02) and μ^* (=10^2) constant.

The reference experiment run for an initially rest mantle condition (U^*= 0) shows that the RT instabilities start to amplify with an appreciable rate (~1) at a model run time, $t \approx 0.052$. The instabilities then grow with exponentially increasing rates to form typical plume structures (bulbous heads trailing into narrow tails) at $t \approx 0.1$ (Fig. 3). At this stage, the plume heads ascend vertically through the mantle at the rates of 14.4 - 18, which is approximately in the same order of magnitudes obtained from the Stokes formula (Turcotte and Schubert, 2002). In a simulation with U^*= ~18 (Fig.S4) the global flow is found to dampen the instability growth in the initial stage, allowing them to grow at a relatively lower rate (~0.84) on a longer time scale ($t \approx 0.067$), and the fastest growing instabilities attain a typical plume structure at $t \approx$

0.13. The dampening effect strengthens further when U^*= ~36, where the instabilities grow in amplitude at much slower rates (~0.72 at $t \approx 0.067$) (Fig. 3) that becomes almost steady with time. Under this kinematic condition the instabilities eventually do not form any typical plume structure even after a very long model run time ($t \approx 0.187$) (Fig. 4).

The CFD simulation results described above clearly suggest that, under a given set of physical parameters, such as A_T, $\mu^*$and layer thickness ratio, horizontal global flows in the mantle can act as a dampening factor in the RT instability dynamics to suppress the process of plume formation in the basal buoyant layer. Fig 4a and b show reducing plume ascent heights and vertical ascent velocities of the fastest growing instabilities with increasing U^*.

2.2.2. Role of source-layer buoyancy

We ran a set of simulations by varying A_T in the range 0.01-0.04 for U^* = 0, keeping μ^*= 10^2. For low buoyancy (A_T = 0.01), the instabilities start to grow in amplitude at significant rates (0.36 at $t \approx 0.089$), and the fastest growing wave forms a typical head-tail structure of the plume at $t \approx 0.149$ that continued to ascend vertically through the mantle layer. Increase in A_T greatly facilitates the RT instability growth as expected, and develops mature plume structures on much shorter time scales, for example, ($t \approx 0.049$) when A_T = 0.03. For a given simulation run time, the growth rate of instabilities increases with increasing A_T (Fig. 5), but showing little variations in their wavelengths. Fig 7a and b present sets of graphical plots to show temporal variations of the ascent height of the fastest growing plumes and their ascent velocity, respectively as a function of A_T.

2.2.3. Effects of source-layer viscosity

We ran another set of simulations by varying the viscosity ratio (μ^*) in the range 10^1 – 10^4 for U^* = 0, assigning A_T = 0.02. For a lower viscosity ratio (μ^* = 10^2), the instabilities are initiated with a non-dimensional wavelength, $\lambda^* = 12 – 15$, and they grow at significant rates (2.4) on a model run time, $t \approx 0.075$ (Fig. 6) and subsequently give rise to plume structures on a time scale of ~0.112. In addition to the fastest growing waves, several secondary waves evolve (Fig S5) into plume structures at relatively shorter wavelengths ($\lambda^* = 300 – 400$). Increasing μ^* facilitates the instability growth rates and thereby reduces the time scale of plume formation (Fig. 6). For example, $\mu^* = 10^4$ yields fastest growing instabilities at $t \approx 0.029$, which form typical head-tail plume structures within a much shorter time scale ($t \approx 0.045$). The spacing of well-developed plumes calculated from these simulations show a nonlinear, but positive correlation with the overburden to source layer viscosity ratio (Fig. S6a). We also investigated the effects of source-layer thickness, normalized to overburden thickness and obtained a similar increase of plume spacing with increasing source-layer thickness (Fig. S6b).

The vertical ascent height of plumes and their corresponding ascent velocities are summarily shown in graphic plots for different μ^* values (Figs. 7c &d). Interestingly, the inverse relations of plume ascent velocity with the source-layer viscosity obtained from our models have been also reported in earlier studies (van Keken *et al.* 1997).

3. Linear stability analysis

3.1. Mathematical formulation

Consider a thin, mechanically distinct layer (source layer) above the CMB, lying below the mantle, subjected to a global horizontal flow, as illustrated in Fig 8. Here we develop the theory based on a thin-layer approximation (Brun et al., 2015), which assumes layer thickness (h_2) much smaller than the length scale of the system. We choose a Cartesian coordinate system, *xz* with the z axis in the vertical direction (positive upward). The thin layer is confined between $z = 0$ and $z = h_2(x, t)$ that represents the interface between the layer and the overlying mantle, respectively. The thin layer is assigned a negative density contrast relative to the overlying mantle region, and the entire system rests upon an undeformable substrate. We consider a layer parallel velocity condition at the interface $z = h_2(x,t)$ that forces materials in the thin layer to advect in the horizontal direction. The linear stability analysis is developed in the framework of mass and momentum conservation conditions, as in the CFD simulations. Considering incompressible fluid in the thin-layer, using Eq. (1) we expand the mass conservation equation as,

$$\frac{\partial v}{\partial z} + \frac{\partial u}{\partial x} = 0, \tag{6}$$

where u and v denote the x- and z components of the flow velocity in the thin-layer, respectively. All the notations and their corresponding physical variables are summarised in Table 1. Applying the thin-layer approximation (Babchin *et al.* 1983), the momentum conservation conditions follow

$$\frac{\partial p}{\partial z} = -\Delta\rho g \tag{7}$$

and

$$\mu_2 \frac{\partial^2 u}{\partial z^2} - \frac{\partial p}{\partial x} = 0, \tag{8}$$

where p is the excess hydrostatic pressure, $\Delta\rho = \rho_1 - \rho_2$ is the density contrast between the denser overlying medium and the lighter thin layer at the base, and μ_2 is the thin-layer viscosity. The differential equations are solved using a set of boundary conditions (BCs) in the following way. The bottom surface is subjected to an impenetrable boundary condition:

$$v|_{z=0} = 0. \tag{9}$$

In addition, assuming a free-slip condition at this boundary, we have

$$\left.\frac{\partial u}{\partial z}\right|_{z=0} = 0. \tag{10}$$

The layer-interface, on the other hand, is subjected to a differential normal stress condition, given by

$$p = p|_{z=h_2} + \Delta\rho g(z - h_2), \tag{11}$$

where $p|_{z=h_2}$ stands for the flow-induced normal stress at the mantle-thin layer interface, and the second term denotes buoyancy-induced pressure. To derive the horizontal velocity component in the thin layer, substituting Eq. (11) in Eq. (8), we have

$$\mu_2 \frac{\partial^2 u}{\partial z^2} - \frac{\partial}{\partial x}(-\Delta\rho g h_2 + p|_{z=h_2}) = 0. \tag{12}$$

On integration and after applying the boundary conditions (Eq. 9, 10), the differential equation (Eq. 12) yields

$$u = u|_{z=h_2} + \frac{1}{2\mu_2}\frac{\partial}{\partial x}(-\Delta\rho g h_2 + p|_{z=h_2})(z^2 - {h_2}^2). \tag{13}$$

The corresponding vertical component is derived from the mass conservation equation (Eq. 6) after applying the impenetrable BC at $z = 0$ (Eq. 9) as,

$$v|_{z=h_2} = u|_{z=h_2}\frac{\partial h_2}{\partial x} - \frac{\partial}{\partial x}\int_0^{h_2} u dz. \tag{14}$$

Substituting Eq. (13) into Eq. (14), we get

$$v|_{z=h_2} + h_2\frac{\partial u|_{z=h_2}}{\partial x} - \frac{\partial}{\partial x}\left[\frac{{h_2}^3}{3\mu_2}\frac{\partial}{\partial x}(-\Delta\rho g h_2 + p|_{z=h_2})\right] = 0. \tag{15}$$

Considering the kinematic boundary condition at the interface,

$$\frac{\partial h_2}{\partial t} = v|_{z=h_2} - u|_{z=h_2}\frac{\partial h_2}{\partial x}, \tag{16}$$

Eq. (15) yields,

$$\frac{\partial h_2}{\partial t} + \frac{\partial}{\partial x}(h_2 u|_{z=h_2}) - \frac{\partial}{\partial x}\left[\frac{{h_2}^3}{3\mu_2}\frac{\partial}{\partial x}\left(-\Delta\rho g h_2 + p|_{z=h_2}\right)\right] = 0. \tag{17}$$

Eq. (17) defines the evolution of the interface, governed by the two competing forces: 1) non-hydrostatic pressure forces arising from the negative density contrast between the thin-layer and the mantle (3rd term) and 2) viscous forces due to the layer-parallel advective flow at the interface (2nd term). We now introduce a horizontal velocity at the interface as

$$u|_{z=h_2} = U_i(x, t) \tag{18}$$

It is to note that the overlying horizontal mantle flows can be perturbed at some incipient geometrical irregularities on the thin layer, producing spatially and temporally heterogeneous layer-parallel flows close to the interface, as revealed from numerical simulations (Fig. 3). We thus generalize this theoretical problem by setting the boundary condition $u|_{z=h_2}$ as a function of *x* and *t*.

The vertical flows in the basal layer develop pure shear components at the interface, the rate of which can be expressed as (Hernlund & Bonati 2019),

$$\dot{\epsilon} = -\left(\frac{\partial v}{\partial z}\right)\bigg|_{z=0}. \tag{19}$$

The corresponding normal stress at the interface follows,

$$p|_{z=h_2} = \mu_1 \dot{\epsilon}, \tag{20}$$

where μ_1 is the viscosity of the overburden layer. The boundary condition (Eq. 18) represents a heterogeneous horizontal mantle flow condition as a function of *x* on the layer interface at a given instant. We choose a sine wave function with a characteristic wavenumber k_M and a characteristic length-scale L to express the spatially varying horizontal interfacial flows. We later show the linear stability analysis in the perspective of different k_M versus *k* (instability wavelength) relations. Now, using the continuity equation (Eq. 6) in Eq. (19), the expression of strain rate at the interface follows,

$$\dot{\epsilon} = -\frac{U_i(x,t)k_M}{2}\cos\left(\frac{k_M x}{2}\right). \tag{21}$$

Substitution of Eq. (21) in Eq. (20) yields the normal stress at the interface as a function of *x*.

By combining Eqs. (17, 20 and 21), we obtain the final equation that expresses the geometrical evolution of the interface between the basal thin layer and the overlying mantle in the presence of a global horizontal flow:

$$\frac{\partial h_2}{\partial t} + \frac{\partial}{\partial x}(h_2 u|_{z=h_2}) + \frac{\partial}{\partial x}\left[\frac{{h_2}^3}{3\mu_2}\frac{\partial}{\partial x}\left(\Delta\rho g h_2 + \mu_1 \frac{U_i k_M}{2}\cos\left(\frac{k_M x}{2}\right)\right)\right] = 0, \tag{22}$$

where U_i stands for the maximum horizontal flow magnitude at the interface, determined by the global horizontal flow velocity in the overlying mantle. At infinitesimal time the interfacial deflection (h_d) is assumed to be small enough such that $h_d \ll \varepsilon h_2$. Under this condition the linear terms determine the growth of instabilities at the interface in the system. The first term within the third bracket in Eq. (22) represents the favoring force, where the density difference ($\Delta\rho$) facilitates the low-density fluid in the thin-layer to push vertically up against the overlying denser mantle. On the other hand, the second term represents the normal stress at the interface set by the large-scale horizontal flow that tends to dampen the instability growth under the boundary condition within the characteristic length (L).

To deal with the mathematical problem, we non-dimensionalize the governing equations and the BCs using the following variables

$$x^* = \frac{x}{L}, z^* = \frac{z}{h_0}, h^* = \frac{h_2}{h_0}, p^* = \frac{p}{\Delta\rho g h_0}, u^* = \frac{u\mu_2}{\Delta\rho g h_0^2},$$
$$v^* = \frac{v\mu_2}{\Delta\rho g h_0^2}\left(\frac{L}{h_0}\right),\ t^* = \frac{\Delta\rho g h_0^2}{\mu_2 L}t, \tag{23}$$

where h_0 is the mean height of the interface. The governing equations then become,

$$\frac{\partial v^*}{\partial z^*} + \frac{\partial u^*}{\partial x^*} = 0, \tag{24}$$

$$\frac{\partial p^*}{\partial z^*} = 1 \tag{25}$$

$$\frac{\partial^2 u^*}{\partial z^{*2}} - \frac{\partial p^*}{\partial x^*} = 0, \tag{26}$$

and the BCs reduce to

$$v^*|_{z^*=0} = 0 \tag{27}$$

$$\left.\frac{\partial u^*}{\partial z^*}\right|_{z^*=0} = 0 \tag{28}$$

$$p^* = p^*|_{z^*=h^*} + (z^* - h^*). \tag{29}$$

With these new variables our interface evolution equation becomes

$$\frac{\partial h^*}{\partial t^*} + \frac{\partial}{\partial x^*}\left(h^* u^* \big|_{z^*=h^*}\right) + \left(\frac{h_0}{L}\right)\frac{\partial}{\partial x^*}\left[\frac{h^{*3}}{3}\frac{\partial}{\partial x^*}\left(h^* + p^*|_{z^*=h^*}\right)\right] = 0, \qquad (30)$$

To derive the dispersion relation of an instability at the interface, we introduce a small perturbation to the mean height of the interface,

$$h_2(x,t) = h_0 + \varepsilon h_d(x,t), \qquad (31)$$

where h_0 is the mean height of the interface and $h_d(x,t)$ represents the perturbation with $\varepsilon \ll 1$. Using Eq. (31) in Eq. (22) and keeping only the $\mathcal{O}(\varepsilon)$ terms, we find

$$\frac{\partial h_d}{\partial t} + \frac{\partial}{\partial x}\left(h_d u|_{z=h_2}\right) + \frac{\partial}{\partial x}\left[\frac{h_0^3}{3\mu_2}\Delta\rho g\frac{\partial h_d}{\partial x} + \frac{\mu_1}{\mu_2}\frac{h_0^2 h_d U_i k_M}{2}\cos\left(\frac{k_M x}{2}\right)\right] = 0 \qquad (32)$$

Note that any perturbation developed at the interface will simultaneously advect in the x-direction in response to the layer-parallel mantle flow. We thus choose a spatio-temporal perturbation in the following form:

$$h_d(x,t) = C \exp i(kx - \omega t), \qquad (33)$$

where C is a pre-factor, k is the perturbation wavenumber, and ω is the angular frequency. Substituting the expression of $h_d(x,t)$ in Eq. (32), and after some algebraic manipulation, we get

$$\omega = ku|_{z=h_2} - i\frac{\partial u|_{z=h_2}}{\partial x} + i\frac{h_0^3}{3\mu_2}\Delta\rho g k^2 + i\frac{h_0^2 k_M^3 U_i}{8}\frac{\mu_1}{\mu_2}\cos\left(\frac{k_M x}{2}\right)$$
$$- \frac{h_0^2 k_M^2 k U_i}{4}\frac{\mu_1}{\mu_2}\sin\left(\frac{k_M x}{2}\right). \qquad (34)$$

This equation provides a dispersion relation for interfacial instability in a complex form. Its imaginary part yields the growth rate as,

$$\sigma = -\frac{\partial u|_{z=h_2}}{\partial x} + \frac{h_0^3}{3\mu_2}\Delta\rho g k^2 + \frac{h_0^2 k_M^3 U_i}{8}\frac{\mu_1}{\mu_2}\cos\left(\frac{k_M x}{2}\right). \qquad (35)$$

Considering the mantle advection model, this equation takes the following form.

$$\sigma = \frac{k_M U_i}{2}\cos\left(\frac{k_M x}{2}\right) + \frac{h_0^3}{3\mu_2}\Delta\rho g k^2 + \frac{h_0^2 k_M^3 U_i}{8}\frac{\mu_1}{\mu_2}\cos\left(\frac{k_M x}{2}\right). \qquad (36)$$

The second term on the RHS of Eq. (36) favors the growth of the instability due the presence of density difference ($\Delta\rho$), the source layer viscosity in the same term on the other hand inhibits the instability growth. The first and third term on the RHS represents the dampening force of velocity. It is to note that the dispersion relation (Eq. 36) in the absence of any external flow ($U_i = 0$) yields the same expression reported from previous stability analyses with thin-layer approximations (Brun *et al.* 2015; Ghosh, Maiti, & Mandal 2020). In terms of non-dimensionalized variables, Eq. (36) takes the following form,

$$\sigma^* = \frac{k_M^* U_i^*}{2} \cos\left(\frac{k_M^* x^*}{2}\right) + \frac{k^{*2}}{3} + \frac{k_M^{*3} U_i^*}{8} \frac{\mu_1}{\mu_2} \cos\left(\frac{k_M^* x^*}{2}\right),$$
$$\sigma^* = \frac{\sigma\mu_2}{\Delta\rho g h_0}, k^* = kh_0. \tag{37}$$

This generalized solution accounts for an initial kinematic heterogeneity (i.e., lateral flow gradient) at the interface between the two layers, which we implement by choosing the velocity boundary condition as a function of x^*. Consequently, the growth of an interfacial instability depends on its location with respect to the heterogeneity configuration, and the growth rate in the dispersion relation becomes a function of x^*. In the foregoing sections we deal with the analytical solution (Eq. 37) for $x^* = 0$ to show exclusively the effect of horizontal flow magnitude (U_i^*) on the instability development.

3.2. Analytical results

We will now use Eq. 37 to study the effects of model parameters on the growth rate σ^* of Rayleigh-Taylor instabilities in the thin layer. We first undertake this study for a condition of comparable k_M^* and k^* values ($k_M^* \sim k^*$), i.e., the length-scale of horizontal flow heterogeneity at the layer interface is close to that of instabilities growing in the thin-layer. The analysis is then extended for a condition, $k_M^* \ll k^*$ which implies the horizontal flow heterogeneity far exceeding the instabilities in length scales. For $k_M^* \sim k^*$, increasing U_i^* (a non-dimensional form of U_i) facilitates the system to become more stable, as reflected from reducing amplitudes of the dispersion curve in Figure 9a. U_i^* also greatly influences the wavenumber k^* corresponding to the most unstable modes, forming an inverse relation of k^* with U_i^*. For example, k^* = 0.5 for U_i^* = 10, which drops to nearly 0.2 at U_i^* = 30. The theoretical results (Fig 9a) suggest that increasing horizontal flow velocity in the mantle favours interfacial instabilities to grow at longer wavelengths, and at the same time dampens their growth rates.

We now consider the second case, $k_M{}^* \ll k^*$ to show the effects of U_i^* on the modes of instability growth in the thin layer from two graphical plots for U_i^* = 20 and 30. We compare these plots with those for $k_M{}^* = k^*$ to find additional influence of the $k_M{}^*$ versus k^* relation. Increase in U_i^* yields similar inverse impacts on both the maximum growth rates and their corresponding wave numbers, irrespective of $k_M{}^* = k^*$ and $k_M{}^* \ll k^*$ conditions. However, for a given U_i^* a transition from $k_M{}^* \ll k^*$ (Fig. 9c, dashed lines) to $k_M{}^* = k^*$(Fig. 9a) condition greatly reduces the dominant wavenumber and its corresponding growth rate, implying that the latter condition is less effective to produce instabilities in the basal thin layer.

The source-layer viscosity μ_2 is another influential factor for the dispersion of various modes, as shown from a set of graphical plots in Figure 9b. For a given U_i^*, the plots indicate that increasing μ_2, relative to the overburden layer viscosity μ_1, significantly dampens the growth rate of the RTIs (Fig. 9b, black and red lines). Secondly, the dominant wavelength of instabilities increases with decreasing source-layer viscosity (shown in the inset of Fig. 9b). The instabilities which grow against the prevalent gravitational forces, undergo significantly more resistance for higher values of source-layer viscosity, leading to the observed dampening effect of μ_2. (Fig. 9b, blue, green lines). We also investigated the effects of source-layer viscosity for the two conditions: $k_M{}^* = k^*$ and $k_M{}^* \ll k^*$ (Fig. 9d). For a given source-layer viscosity μ_2, a change in the condition from $k_M{}^* = k^*$ and $k_M{}^* \ll k^*$ reduces the amplitude (maximum growth rate) of dispersion relations and their corresponding wavenumbers (Fig. 9d, dashed lines).

Using Eq. 36 we studied the evolution of interfacial instabilities as a function of the initial source-layer thickness h_0. Increasing h_0 facilitates their growth rate because the destabilizing force (second term in the equation) is proportional to h_0^3. Detailed analysis of the effect of h_0 is presented in Supplementary S7.

4. Discussions

4.1. RTI simulations and theoretical predictions: a synthesis

This study primarily shows that an interface-parallel velocity in horizontally stratified fluid layers of inverted densities results in significant dampening of the RT instabilities in the layered systems, where their growth rate is found to be inversely related to the interface-parallel velocity magnitude (U^*). Our CFD simulations suggest that, under a given set of physical parameters, e.g., A_T = 0.02, μ^* =10^2, and h_2 = 0.045 (equivalent to an absolute thickness of 100km), $U^* \geq 18$ can noticeably dampen the growth of RT instabilities, completely suppressing them to amplify into plume structures at a threshold U^*. The model parameters chosen in this study yield the threshold state at U^* ~36 (Fig. 4a, b). It is noteworthy that the threshold magnitude of the layer-parallel flow depends on the physical setting of the layered system defined by various parameters, such as Atwood number (A_T), viscosity ratio, source-layer thickness and initial geometrical heterogeneities (ΔA) at the layer interface. As an example, a system with large A_T would require a much higher threshold U^* value to absolutely dampen the instability growth. Similar effects can occur in case of a layer system containing high-amplitude interfacial perturbations (i.e., large ΔA values). The linear stability analysis also predicts dampening effects of strong global flows on the growth of instabilities, and the existence of a threshold flow magnitude at which no instability growth occurs (Fig. 9a). In addition, the theoretical results suggest that the global flow significantly influences the preferred wavelength at which RT instabilities can dominantly grow. Low layer-parallel velocities, e. g., $U_i^* \sim 10$, dampen selectively instability of shorter wavelengths, i.e., of higher wavenumbers (Fig. 9a). Consequently, ambient velocity fields, in general, facilitate RT instabilities to grow on longer wavelengths in preference to those on shorter wavelengths. The theoretical prediction implies that the ambient mantle flows reduce the spatial frequency of plumes, allowing them to form at a large horizontal spacing, as reflected in the sporadic distributions of plume-driven hotspots.

We dealt with the Atwood number A_T in our CFD simulations, aiming to evaluate the effects of density contrast, $\Delta\rho = \rho_1 - \rho_2$ between the source layer and the overlying mantle. The density contrast is an important factor in the context of our present problem as the lower mantle is compositionally as well thermally heterogeneous (Davies *et al.* 2012; Farnetani *et al.* 2018), and such heterogeneities can eventually give rise to a large spatial variation in $\Delta\rho$. The simulation results suggest a positive relation of the instability growth rate with density contrast, as also predicted by earlier studies (van Keken *et al.* 1997) and the present stability analysis (Eq. 36), implying that increasing density contrast favours instabilities to amplify at fast rates (Fig. 7a, b). This finding allows us to hypothesize that inherent heterogeneities can be an important factor in preferential growth of mantle plumes initiated by RT instabilities. Thermo-chemical heterogeneities in mantle, e.g., TBL piling, can also result in lateral variations of the mantle viscosity, as reported from seismic tomographic studies (McNamara & Zhong 2004, Davaille & Romanowicz 2020). Our analytical solution shows that the wavelength of RT instabilities increases nonlinearly with the mantle/source-layer viscosity ratio ($\frac{\mu_1}{\mu_2}$) (Fig. 10b), as shown in earlier studies (Lister & Kerr 1989). The result suggests that the number of possible plume instabilities in a mantle region with large $\frac{\mu_1}{\mu_2}$ ratios should be low, but they will grow at fast rate$s$; that means, under a given mantle viscosity condition lowering of the source-layer viscosity facilitates the growth rate of RT instabilities, as evident from the dispersion relations shown in Fig. 9c.

4.2. Impact of global flows on RT instability: geodynamic perspectives

Earlier theoretical and experimental studies have extensively investigated the evolution of mantle plumes originated from deep mantle sources by RT instabilities. However, how the presence of a global horizontal flow in the mantle that may originate from various geodynamic processes, such as thermal convection (Olson *et al.* 1990), subducting slab driven shear flows (Čížková *et al.* 2012; van der Meer *et al.* 2018), and mantle winds (Tarduno *et al.* 2009) (Fig. 1), can influence the instability growth dynamics demands a quantitative analysis, which is the principal focus of this article. Previous model estimates suggest that subducting slabs sink in the lower mantle with velocity magnitudes in the range 1-4 cm/yr at the top to 1-2 cm/yr at the mid-mantle depths (van der Meer *et al.* 2018), whereas the maximum root-mean-square vector velocity field for whole mantle convection is estimated around 30 cm/yr (Knopoff 1964) where Rayleigh number in the order of 10^8. Our reference CFD simulation ($U^* = 0$) provides an estimate of 1 – 2 cm/yr for the initial growth rate of instabilities in the source layer. The global ambient flows in the overlying mantle can thus greatly influence the process of plume initiation at the TBL. In fact, some model studies have recently shown that such global flows can force ascending plumes to deflect from the vertical trajectories (Kerr & Mériaux 2004; Kerr *et al.* 2008; Hassan *et al.* 2016), as documented from the seismic tomography of natural plumes, e.g., the Hawaiian plume is strongly deflected towards the west–southwest at around 1000 km depth (French & Romanowicz 2015; Lei *et al.* 2020). However, these studies entirely focus on the interaction of mature plumes with global horizontal flows, giving little attention to the problem of plume initiation in a source layer, which fundamentally determines the possibility of plume formation in a geodynamic setting. The linear stability analysis also suggests that the horizontal global flows in the mantle can critically control the initiation of plume instabilities in buoyant source layers. In extreme conditions they can completely suppress the instabilities, allowing no plume to evolve in the system. For a mechanical setting with $A_T = 0.01$ and $\mu^* = 10^1$, instabilities that can amplify at a velocity of ~0.2-0.3 cm/yr in a rest mantle condition, are effectively suppressed if the mantle flows attain a threshold condition ($U^* \geq 36$, i.e., 7-10 cm/yr in the absolute scale). This RT instability mechanics is applicable to several other geodynamic settings, which is briefly discussed below.

4.3. Magmatic hotspots on Earth's surface: some questions

Morgan (1971) in his seminal work proposed deep-mantle plumes as the principal source of primary magmatic hotspots, but their origin still remains a subject of great debate (Koppers *et al.* 2021). Later studies have proposed a set of criteria in support of the deep-mantle hypothesis for hotspots: a) linear chain of volcanoes with monotonous age progression, b) flood basalt at the origin of this track, c) a large buoyancy flux, d) the presence of consistently high ratios of three to four helium isotopes, and e) occurrence of large low-shear-velocity provinces (LLSVPs) at the base of lower mantle. Based on these criteria, it has been possible to ascertain the following nine hotspots of deep-mantle origin: Hawaii, Pitcairn, Samoa and Louisville (Jellinek & Manga 2004; Koppers *et al.* 2021) in the Pacific hemisphere and Iceland, Afar, Reunion, Tristan and Kerguelen in the Indo-Atlantic hemisphere (Fig. 11). Their spatial distribution reveals that these hotspots are located at large distances from one another. For example, the Hawaii chain and the Samoan hotspot are located ~5000 km away from each other. Similarly, the Iceland and the Tristan hotspots maintain a spacing, more than 8000 km. On contrary, experimental and theoretical studies (Montague & Kellogg 2000) show mantle plumes generated in the TBL at the CMB at much smaller wavelengths, lying in the range 1400 km to 1800 km. The plume frequency observed in experimental models evidently holds a clear disagreement with the spatial density of deep-mantle hotspots across the globe. This disagreement poses the following critical question- why are hotspots of deep-mantle plume origin so rare on the earth surface?

One of the reasonable ways to address this crucial question is to find some geodynamic phenomena that can counter the plume initiation process in the TBL above the CMB, allowing a few plumes to grow in the mantle and produce sporadic hotspots. Recent studies (Li *et al.* 2018; McNamara 2019; Koppers *et al.* 2021) have hypothesized a linkage between LLSVPs, mantle plumes and hotspots, where the LLSVPs act as source regions of deep-mantle plume formation. From geophysical observations Thorne et al. (2004) proposed that hotspots originate selectively from the LLSVP margins than their interiors. Such a spatial constraint could result in plume formation with large separations, leading to their manifestation as sporadic hotspots. Li and Zhong (2017), on the other hand, have provided a different insight into the problem of wide plume spacing, showing that thickening of the underlying thermal boundary layer (TBL) is an influential factor to determine the plume location preferentially in regions attaining a critical TBL thickness. The present article identifies global horizontal mantle flows as another potential dampening factor for mantle plume initiation. The linear stability analysis shows that the RT instability growth rate becomes negligibly small ($\sigma^* \sim 0$) when the interface parallel flow velocity is significant (U_i^*= ~20). The same global flow effect is observed in the CFD simulations, where the growth rate drops significantly due to imposition of a global flow U^* = >18 (Fig. 3b). The simulation results imply that mantle plumes to ascend to the surface in the flowing mantle states would require an unusually large time scale (>100 Ma on the absolute scale). The mantle flows can also control their spatial frequency preferentially in the flow direction, as revealed from the instability wavenumber (k^*) analysis as a function of U_i^*. k^* corresponding to the fastest growing waves holds an inverse relation with U_i^*, implying that their wavelengths (λ^*) increase with increasing U_i^* (Fig.10a). Applying this theoretical result to a natural equivalent system, it appears that the wavelength of instabilities in a layer of 100 km thickness would be ~250 km in case of rest mantle condition, which multiplies by 10-14 times when the mantle is subjected to a global flow condition of 5 cm/yr. Our instability theory thus provides a possible explanation to the problem of large spacing, i.e. low frequency of volcanic hotspots in the light of RT instability mechanics.

4.4. Model limitations

Both the numerical models and the theory presented in this article have a number of limitations. 1) Both of them are developed in the framework of a mechanical approach, without considering the thermal effects. This assumption was adopted to focus upon the ambient mantle flows as the factor of our main concern in the analysis of RT instabilities. Moreover, the present model is developed entirely within the framework of linear viscous rheology. Evidently, there is a need to explore temperature and non-linear viscous rheology as additional factors in the modelling. 2) The model viscosity is held constant to represent the average mechanical state of lower mantle. Thus, there is a scope for investigating the possible effect of rheological stratification in the mantle and depth-dependent mineral phase transformations. 3) The theory linearizes the problem, excluding the non-linear terms. This approach limits us from performing an analysis for time dependent plume growth. This difference possibly results from the thin-layer approximation chosen in the theory. Furthermore, the present study is based on a 2D modelling approach, considering that the system contains irregularities at the layer interface with extremely low initial amplitudes, and thereby develops negligibly small velocity perturbations across the global flow direction. However, a 3D model study is required to generalize the problem for mechanical systems with initially large-amplitude geometrical irregularities at the interface. Finally, the present theoretical formulation excludes complex processes, such as piling at TBL, as shown by previous workers (Heyn *et al.* 2018).

5. Summary and conclusions

This article reports the role of horizontal global flows in controlling RT instabilities in a buoyant source layer beneath a heavier fluid medium, and addresses the problem of plume formation in the TBL above the CMB earth's mantle. Combining CFD simulation results with a linear stability analysis, this study finally leads to the following conclusions. 1) The global flows always dampen the growth of RT instabilities, where the degree of dampening can vary depending on the initial physical setting of a two-layer system. Under a given initial condition, the system will completely impede the instabilities to grow into a characteristic plume structure at a threshold flow velocity. 2) The linear stability analysis confirms the dampening effects of global flow velocity on the instability growth, predicting that the layer-parallel mantle flow velocities > 30 times the initial plume ascent velocity suppress short as well as long-wave instabilities. The analysis also reveals that increasing normalized ambient velocity (10 to 30) causes the instabilities to increase their dominant wavelengths (10 to 40), normalized to the initial layer thickness. 3) The theory also predicts the effects of additional factors: density ratio, source-layer viscosity and layer thickness on the growth rate of an instability in an RTI system. All the three physical parameters act as a driving role in facilitating the instability growth rate. 4) The dampening effects of global flows established in this study can explain the mechanics of plume generation in various geodynamic settings, such as subduction zones and the 660 km transition zone. Finally, the theory provides a potential explanation for spatially distant primary mantle plumes, manifested in the form of a few hotspots on earth's surface.

Acknowledgements

We thank Dr. Cedric Thieulot and two anonymous reviewers for their incisive comments and constructive suggestions that greatly helped us to refine this study. We also thank Editors Prof. Gael Choblet and Dr. Ian Bastow for their editorial handling of our manuscript. A.R. gratefully acknowledges CSIR, India for awarding research fellowship grants (09/096(0940)/2018-EMR-I) and D. G. acknowledges UGC for Senior Research Fellowship. This work used the ARCHER2 UK National Supercomputing Service (https://www.archer2.ac.uk). The DST-SERB is acknowledged for supporting this work through the J.C. Bose fellowship (SR/S2/JCB-36/2012) to N.M.

Data Availability Statement

The authors confirm that all the data used to support the findings of this study are available within the article and as supplementary materials.

References

Babchin, A.J., Frenkel, A.L., Levich, B.G. & Sivashinsky, G.I., 1983. Nonlinear saturation of Rayleigh-Taylor instability in thin films. *Physics of Fluids*, **26**. doi:10.1063/1.864083

Baldwin, K.A., Scase, M.M. & Hill, R.J.A., 2015. The inhibition of the Rayleigh-Taylor instability by rotation. *Sci Rep*, **5**, Nature Publishing Group. doi:10.1038/srep11706

Ballmer, M.D., Ito, G., Hunen, J. Van & Tackley, P.J., 2011. Spatial and temporal variability in Hawaiian hotspot volcanism induced by small-scale convection. *Nat Geosci*, **4**, 457–460. doi:10.1038/NGEO1187

Bekaert, D. v., Gazel, E., Turner, S., Behn, M.D., Moor, J.M. de, Zahirovic, S., Manea, V.C., *et al.*, 2021. High 3He/4He in central Panama reveals a distal connection to the Galapagos plume. *Proc Natl Acad Sci U S A*, **118**, e2110997118, National Academy of Sciences. doi:10.1073/PNAS.2110997118/SUPPL_FILE/PNAS.2110997118.SD03.XLSX

Bercovici, D. & Kelly, A., 1997. The non-linear initiation of diapirs and plume heads. *Physics of the Earth and Planetary Interiors*, **101**. doi:10.1016/S0031-9201(96)03217-7

Bredow, E., Steinberger, B., Gassmöller, R. & Dannberg, J., 2017. How plume-ridge interaction shapes the crustal thickness pattern of the Réunion hotspot track. *Geochemistry, Geophysics, Geosystems*, **18**, 2930–2948. doi:10.1002/2017GC006875

Bredow, E., Steinberger, B., Gassmöller, R. & Dannberg, J., 2023. Mantle convection and possible mantle plumes beneath Antarctica – insights from geodynamic models and implications for topography. *Geological Society, London, Memoirs*, **56**, 253–266, Geological Society of London. doi:10.1144/M56-2020-2

Brun, P.T., Damiano, A., Rieu, P., Balestra, G. & Gallaire, F., 2015. Rayleigh-Taylor instability under an inclined plane. *Physics of Fluids*, **27**. doi:10.1063/1.4927857

Brunet, D. & Yuen, D.A., 2000. Mantle plumes pinched in the transition zone. *Earth Planet Sci Lett*, **178**, 13–27, Elsevier. doi:10.1016/S0012-821X(00)00063-7

Burcet, M., Oliveira, B., Afonso, J.C. & Zlotnik, S., 2023. A face-centred finite volume approach for coupled transport phenomena and fluid flow. *Appl Math Model*, Elsevier. doi:10.1016/J.APM.2023.08.031

Burke, K., Steinberger, B., Torsvik, T.H. & Smethurst, M.A., 2008. Plume Generation Zones at the margins of Large Low Shear Velocity Provinces on the core–mantle boundary. *Earth Planet Sci Lett*, **265**, 49–60, Elsevier. doi:10.1016/J.EPSL.2007.09.042

Cathles, L.M., 1975. The viscosity of the earth's mantle. *Published in **1975** in Princeton NJ) by Princeton university press*, 413, Princeton (N.J.) : Princeton university press, 1975. Retrieved from https://lib.ugent.be/catalog/rug01:001350016

Čížková, H., Berg, A.P. van den, Spakman, W. & Matyska, C., 2012. The viscosity of Earth's lower mantle inferred from sinking speed of subducted lithosphere. *Physics of the Earth and Planetary Interiors*, **200–201**, 56–62, Elsevier. doi:10.1016/J.PEPI.2012.02.010

Conrad, C.P. & Molnar, P., 1997. The growth of Rayleigh-Taylor-type instabilities in the lithosphere for various rheological and density structures. *Geophys J Int*, **129**, 95–112, Oxford University Press. doi:10.1111/J.1365-246X.1997.TB00939.X

Davaille, A., Carrez, P. & Cordier, P., 2018. Fat Plumes May Reflect the Complex Rheology of the Lower Mantle. *Geophys Res Lett*, **45**, 1349–1354, John Wiley & Sons, Ltd. doi:10.1002/2017GL076575

Davaille, Anne & Romanowicz, B., 2020. Deflating the LLSVPs: Bundles of Mantle Thermochemical Plumes Rather Than Thick Stagnant "Piles". *Tectonics*, **39**, e2020TC006265, John Wiley & Sons, Ltd. doi:10.1029/2020TC006265

Davaille, Anne & Vatteville, J., 2005. On the transient nature of mantle plumes. *Geophys Res Lett*, **32**, 1–4, John Wiley & Sons, Ltd. doi:10.1029/2005GL023029

Davies, D.R., Goes, S., Davies, J.H., Schuberth, B.S.A., Bunge, H.P. & Ritsema, J., 2012. Reconciling dynamic and seismic models of Earth's lower mantle: The dominant role of thermal heterogeneity. *Earth Planet Sci Lett*, **353–354**, 253–269, Elsevier. doi:10.1016/J.EPSL.2012.08.016

Dutta, U., Baruah, A. & Mandal, N., 2016. Role of source-layer tilts in the axi-asymmetric growth of diapirs triggered by a Rayleigh–Taylor instability. *Geophys J Int*, **206**, 1814–1830, Oxford Academic. doi:10.1093/GJI/GGW244

Evans, M., Harlow, F. & Bromberg, E., 1957. The Particle-In-Cell Method for Hydrodynamic Calculations. Retrieved from https://apps.dtic.mil/sti/citations/ADA384618

Farnetani, C.G., Hofmann, A.W., Duvernay, T. & Limare, A., 2018. Dynamics of rheological heterogeneities in mantle plumes. *Earth Planet Sci Lett*, **499**, 74–82, Elsevier B.V. doi:10.1016/j.epsl.2018.07.022

Frazer, W.D. & Korenaga, J., 2022. Dynamic topography and the nature of deep thick plumes. *Earth Planet Sci Lett*, **578**, Elsevier B.V. doi:10.1016/j.epsl.2021.117286

French, S.W. & Romanowicz, B., 2015. Broad plumes rooted at the base of the Earth's mantle beneath major hotspots. *Nature 2015 525:7567*, **525**, 95–99, Nature Publishing Group. doi:10.1038/nature14876

Gerashchenko, S. & Livescu, D., 2016. Viscous effects on the Rayleigh-Taylor instability with background temperature gradient. *Phys Plasmas*, **23**, 072121, AIP Publishing LLCAIP Publishing. doi:10.1063/1.4959810

Gerya, T., 2009. *Introduction to numerical geodynamic modelling*. *Introduction to Numerical Geodynamic Modelling*, Vol. 9780521887540. doi:10.1017/CBO9780511809101

Gerya, T., 2019. Introduction to numerical geodynamic modelling, *Second Edition*. doi:10.1017/9781316534243

Gerya, T. v. & Yuen, D.A., 2003. Rayleigh–Taylor instabilities from hydration and melting propel 'cold plumes' at subduction zones. *Earth Planet Sci Lett*, **212**, 47–62, Elsevier. doi:10.1016/S0012-821X(03)00265-6

Ghosh, D., Maiti, G. & Mandal, N., 2020. Slab-parallel advection versus Rayleigh-Taylor instabilities in melt-rich layers in subduction zones: A criticality analysis. *Physics of the Earth and Planetary Interiors*, **307**, Elsevier B.V. doi:10.1016/j.pepi.2020.106560

Ghosh, D., Maiti, G., Mandal, N. & Baruah, A., 2020. Cold Plumes Initiated by Rayleigh-Taylor Instabilities in Subduction Zones, and Their Characteristic Volcanic Distributions: The Role of Slab Dip. *J Geophys Res Solid Earth*, **125**, Blackwell Publishing Ltd. doi:10.1029/2020JB019814

Griffiths, R.W. & Richards, M.A., 1989. The adjustment of mantle plumes to changes in plate motion. *Geophys Res Lett*, **16**, 437–440, John Wiley & Sons, Ltd. doi:10.1029/GL016I005P00437

Hassan, R., Müller, R.D., Gurnis, M., Williams, S.E. & Flament, N., 2016. A rapid burst in hotspot motion through the interaction of tectonics and deep mantle flow. *Nature 2016 533:7602*, **533**, 239–242, Nature Publishing Group. doi:10.1038/nature17422

Hernlund, J.W. & Bonati, I., 2019. Modeling Ultralow Velocity Zones as a Thin Chemically Distinct Dense Layer at the Core-Mantle Boundary. *J Geophys Res Solid Earth*, **124**, 7902–7917, John Wiley & Sons, Ltd. doi:10.1029/2018JB017218

Heyn, B.H., Conrad, C.P. & Trønnes, R.G., 2018. Stabilizing Effect of Compositional Viscosity Contrasts on Thermochemical Piles. *Geophys Res Lett*. doi:10.1029/2018GL078799

Hillebrand, B., Thieulot, C., Geenen, T., Berg, A.P. Van Den & Spakman, W., 2014. Using the level set method in geodynamical modeling of multi-material flows and Earth's free surface. *Solid Earth*, **5**, 1087–1098, Copernicus GmbH. doi:10.5194/SE-5-1087-2014

Houseman, G.A. & Molnar, P., 1997. Gravitational (Rayleigh-Taylor) instability of a layer with non-linear viscosity and convective thinning of continental lithosphere. *Geophys J Int*, **128**, 125–150, John Wiley & Sons, Ltd. doi:10.1111/J.1365-246X.1997.TB04075.X

Ida, S., Nakagawa, Y. & Nakazawa, K., 1987. The Earth's core formation due to the Rayleigh-Taylor instability. *Icarus*, **69**, 239–248, Academic Press. doi:10.1016/0019-1035(87)90103-5

Jellinek, A.M., Lenardic, A. & Manga, M., 2002. The influence of interior mantle temperature on the structure of plumes: Heads for Venus, Tails for the Earth. *Geophys Res Lett*, **29**, 27–1, John Wiley & Sons, Ltd. doi:10.1029/2001GL014624

Jellinek, A.M. & Manga, M., 2004. LINKS BETWEEN LONG-LIVED HOT SPOTS, MANTLE PLUMES, D″, AND PLATE TECTONICS. *Reviews of Geophysics*, **42**, John Wiley & Sons, Ltd. doi:10.1029/2003RG000144

Jones, T.D., Davies, D.R., Campbell, I.H., Wilson, C.R. & Kramer, S.C., 2016. Do mantle plumes preserve the heterogeneous structure of their deep-mantle source? *Earth Planet Sci Lett*, **434**, 10–17, Elsevier. doi:10.1016/J.EPSL.2015.11.016

Keken, P.E. van, King, S.D., Schmeling, H., Christensen, U.R., Neumeister, D. & Doin, M.-P., 1997. A comparison of methods for the modeling of thermochemical convection. *J Geophys Res Solid Earth*, **102**, 22477–22495, American Geophysical Union (AGU). doi:10.1029/97jb01353

Kerr, R.C., Lister, J.R., Kerr, R.C. & Lister, J.R., 2008. Rise and deflection of mantle plume tails. *Geochemistry, Geophysics, Geosystems*, **9**, 10004, John Wiley & Sons, Ltd. doi:10.1029/2008GC002124

Kerr, R.C. & Mériaux, C., 2004. Structure and dynamics of sheared mantle plumes. *Geochemistry, Geophysics, Geosystems*, **5**. doi:10.1029/2004GC000749

Knopoff, L., 1964. The convection current hypothesis. *Reviews of Geophysics*, **2**, 89–122, John Wiley & Sons, Ltd. doi:10.1029/RG002I001P00089

Koppers, A.A.P., Becker, T.W., Jackson, M.G., Konrad, K., Müller, R.D., Romanowicz, B., Steinberger, B., *et al.*, 2021. Mantle plumes and their role in Earth processes. *Nature*

Reviews Earth & Environment 2021 2:6, **2**, 382–401, Nature Publishing Group. doi:10.1038/s43017-021-00168-6

Korenaga, J., 2005. Firm mantle plumes and the nature of the core-mantle boundary region. *Earth Planet Sci Lett*. doi:10.1016/j.epsl.2005.01.016

Kumagai, I., Davaille, A. & Kurita, K., 2007. On the fate of thermally buoyant mantle plumes at density interfaces. *Earth Planet Sci Lett*, **254**, 180–193, Elsevier. doi:10.1016/J.EPSL.2006.11.029

Lei, W., Ruan, Y., Bozdağ, E., Peter, D., Lefebvre, M., Komatitsch, D., Tromp, J., *et al.*, 2020. Global adjoint tomography—model GLAD-M25. *Geophys J Int*, **223**, 1–21, Oxford Academic. doi:10.1093/GJI/GGAA253

Li, M. & Zhong, S., 2017. The source location of mantle plumes from 3D spherical models of mantle convection. *Earth Planet Sci Lett*, **478**, 47–57, Elsevier. doi:10.1016/J.EPSL.2017.08.033

Li, M., Zhong, S. & Olson, P., 2018. Linking lowermost mantle structure, core-mantle boundary heat flux and mantle plume formation. *Physics of the Earth and Planetary Interiors*, **277**, 10–29, Elsevier. doi:10.1016/J.PEPI.2018.01.010

Lister, J.R. & Kerr, R.C., 1989. The effect of geometry on the gravitational instability of a buoyant region of viscous fluid. *J Fluid Mech*, **202**. doi:10.1017/S0022112089001308

Louis-Napoleon, A., Bonometti, T., Gerbault, M., Martin, R. & Vanderhaeghe, O., 2022. Models of convection and segregation in heterogeneous partially molten crustal roots with a VOF method – I: flow regimes. *Geophys J Int*, **229**, 2047–2080, Oxford Academic. doi:10.1093/GJI/GGAB510

Louis-Napoléon, A., Gerbault, M., Bonometti, T., Thieulot, C., Martin, R. & Vanderhaeghe, O., 2020. 3-D numerical modelling of crustal polydiapirs with volume-of-fluid methods. *Geophys J Int*, **222**, 474–506, Oxford Academic. doi:10.1093/GJI/GGAA141

Lowman, J.P., King, S.D. & Gable, C.W., 2004. Steady plumes in viscously stratified, vigorously convecting, three-dimensional numerical mantle convection models with mobile plates. *Geochemistry, Geophysics, Geosystems*, **5**. doi:10.1029/2003GC000583

Mansour, J., Giordani, J., Moresi, L., Beucher, R., Kaluza, O., Velic, M., Farrington, R., *et al.*, 2020. Underworld2: Python Geodynamics Modelling for Desktop, HPC and Cloud. *J Open Source Softw*, **5**, 1797, The Open Journal. doi:10.21105/joss.01797

Masse, L., 2007. Stabilizing effect of anisotropic thermal diffusion on the ablative Rayleigh-Taylor instability. *Phys Rev Lett*, **98**, 245001, American Physical Society. doi:10.1103/PHYSREVLETT.98.245001/FIGURES/5/MEDIUM

McNamara, A.K., 2019. A review of large low shear velocity provinces and ultra low velocity zones. *Tectonophysics*, **760**, 199–220, Elsevier. doi:10.1016/J.TECTO.2018.04.015

McNamara, A.K. & Zhong, S., 2004. Thermochemical structures within a spherical mantle: Superplumes or piles? *J Geophys Res Solid Earth*, **109**, 7402, John Wiley & Sons, Ltd. doi:10.1029/2003JB002847

Meer, D.G. van der, Hinsbergen, D.J.J. van & Spakman, W., 2018. Atlas of the underworld: Slab remnants in the mantle, their sinking history, and a new outlook on lower mantle viscosity. *Tectonophysics*, **723**, 309–448, Elsevier. doi:10.1016/J.TECTO.2017.10.004

Mikaelian, K.O., 1996. Rayleigh-Taylor instability in finite-thickness fluids with viscosity and surface tension. *Phys Rev E*, **54**, 3676, American Physical Society. doi:10.1103/PhysRevE.54.3676

Miller, N.C. & Behn, M.D., 2012. Timescales for the growth of sediment diapirs in subduction zones. *Geophys J Int*, **190**, 1361–1377, John Wiley & Sons, Ltd. doi:10.1111/J.1365-246X.2012.05565.X

Mondal, P. & Korenaga, J., 2018. The Rayleigh–Taylor instability in a self-gravitating two-layer viscous sphere. *Geophys J Int*, **212**, 1859–1867, Oxford Academic. doi:10.1093/GJI/GGX507

Montague, N.L. & Kellogg, L.H., 2000. Numerical models of a dense layer at the base of the mantle and implications for the geodynamics of D″. *J Geophys Res Solid Earth*, **105**, 11101–11114, Blackwell Publishing Ltd. doi:10.1029/1999JB900450

Moresi, L., Quenette, S., Lemiale, V., Mériaux, C., Appelbe, B. & Mühlhaus, H.B., 2007. Computational approaches to studying non-linear dynamics of the crust and mantle. *Physics of the Earth and Planetary Interiors*. doi:10.1016/j.pepi.2007.06.009

Morgan, W. J., 1971. Convection Plumes in the Lower Mantle. *Nature 1971 230:5288*, **230**, 42–43, Nature Publishing Group. doi:10.1038/230042a0

Morgan, W. Jason, 1972. Deep Mantle Convection Plumes and Plate Motions. *Am Assoc Pet Geol Bull*, **56**, 203–213, American Association of Petroleum Geologists. Retrieved from http://archives.datapages.com/data/bulletns/1971-73/data/pg/0056/0002/0200/0203.htm

Munro, D.H., 1988. Analytic solutions for Rayleigh-Taylor growth rates in smooth density gradients. *Phys Rev A (Coll Park)*, **38**, 1433, American Physical Society. doi:10.1103/PhysRevA.38.1433

Nakada, M., Iriguchi, C. & Karato, S. ichiro, 2012. The viscosity structure of the D″ layer of the Earth’s mantle inferred from the analysis of Chandler wobble and tidal deformation. *Physics of the Earth and Planetary Interiors*, **208–209**, 11–24, Elsevier. doi:10.1016/J.PEPI.2012.07.002

Negredo, A.M., Hunen, J. van, Rodríguez-González, J. & Fullea, J., 2022. On the origin of the Canary Islands: Insights from mantle convection modelling. *Earth Planet Sci Lett*, **584**, 117506, Elsevier. doi:10.1016/J.EPSL.2022.117506

Neil, E.A. & Houseman, G.A., 1999. Rayleigh–Taylor instability of the upper mantle and its role in intraplate orogeny. *Geophys J Int*, **138**, 89–107, Oxford Academic. doi:10.1046/J.1365-246X.1999.00841.X

Nipin, L. & Tomar, G., 2015. Effect of viscosity contrast on plume formation in density stratified fluids. *Chem Eng Sci*, **134**, 510–520. doi:10.1016/j.ces.2015.05.044

Nolet, G., Allen, R. & Zhao, D., 2007. Mantle plume tomography. *Chem Geol*, **241**, 248–263, Elsevier. doi:10.1016/J.CHEMGEO.2007.01.022

Olson, P., Silver, P.G. & Carlson, R.W., 1990. The large-scale structure of convection in the Earth’s mantle. *Nature 1990 344:6263*, **344**, 209–215, Nature Publishing Group. doi:10.1038/344209a0

Olson, P. & Singer, H., 1985. Creeping plumes. *J Fluid Mech*, **158**. doi:10.1017/S0022112085002749

Pullin, D.I., 1982. Numerical studies of surface-tension effects in nonlinear Kelvin–Helmholtz and Rayleigh–Taylor instability. *J Fluid Mech*, **119**, 507–532, Cambridge University Press. doi:10.1017/S0022112082001463

Ramberg, H., 1968. Instability of layered systems in the field of gravity. I. *Physics of the Earth and Planetary Interiors*, **1**, 427–447, Elsevier. doi:10.1016/0031-9201(68)90014-9

Ramberg, H., 1968. Instability of layered systems in the field of gravity. II. *Physics of the Earth and Planetary Interiors*, **1**, 448–474, Elsevier. doi:10.1016/0031-9201(68)90015-0

Ramberg, H., 1972. Theoretical models of density stratification and diapirism in the Earth. *J Geophys Res*, **77**, 877–889, John Wiley & Sons, Ltd. doi:10.1029/JB077I005P00877

Rayleigh, 1882. Investigation of the Character of the Equilibrium of an Incompressible Heavy Fluid of Variable Density. *Proceedings of the London Mathematical Society*, **s1-14**, 170–177, Oxford Academic. doi:10.1112/PLMS/S1-14.1.170

Richards, M. A. & Hager, B.H., 1984. Geoid anomalies in a dynamic earth. *J. geophys. Res.*, **89**, 5987–6002. doi:10.1029/jb089ib07p05987
Richards, Mark A. & Griffiths, R.W., 1989. Thermal entrainment by deflected mantle plumes. *Nature 1989 342:6252*, **342**, 900–902, Nature Publishing Group. doi:10.1038/342900a0
Roy, A., Roy, N., Saha, P. & Mandal, N., 2021. Factors Determining Shear-Parallel Versus Low-Angle Shear Band Localization in Shear Deformations: Laboratory Experiments and Numerical Simulations. *J Geophys Res Solid Earth*, **126**, e2021JB022578, John Wiley & Sons, Ltd. doi:10.1029/2021JB022578
Roy, N., Roy, A., Saha, P. & Mandal, N., 2022. On the origin of shear-band network patterns in ductile shear zones. *Proceedings of the Royal Society A*, **478**, The Royal Society. doi:10.1098/RSPA.2022.0146
Samuel, H. & Evonuk, M., 2010. Modeling advection in geophysical flows with particle level sets. *Geochemistry, Geophysics, Geosystems*, **11**, 8020, John Wiley & Sons, Ltd. doi:10.1029/2010GC003081
Song, Y., Wang, P. & Wang, L., 2021. Numerical investigations of Rayleigh–Taylor instability with a density gradient layer. *Comput Fluids*, **220**, 104869, Pergamon. doi:10.1016/J.COMPFLUID.2021.104869
Spada, G., Yuen, D.A., Sabadini, R. & Boschi, E., 1991. Lower-mantle viscosity constrained by seismicity around deglaciated regions. *Nature 1991 351:6321*, **351**, 53–55, Nature Publishing Group. doi:10.1038/351053a0
Steinberger, B. & O'Connell, R.J., 1998. Advection of plumes in mantle flow: Implications for hotspot motion, mantle viscosity and plume distribution. *Geophys J Int*, **132**, 412–434, Oxford University Press. doi:10.1046/j.1365-246x.1998.00447.x
Styles, E., Goes, S., Keken, P.E. van, Ritsema, J. & Smith, H., 2011. Synthetic images of dynamically predicted plumes and comparison with a global tomographic model. *Earth Planet Sci Lett*, **311**, 351–363, Elsevier. doi:10.1016/J.EPSL.2011.09.012
Tackley, P.J. & King, S.D., 2003. Testing the tracer ratio method for modeling active compositional fields in mantle convection simulations. *Geochemistry, Geophysics, Geosystems*, **4**, John Wiley & Sons, Ltd. doi:10.1029/2001GC000214
Tarduno, J., Bunge, H.P., Sleep, N. & Hansen, U., 2009. The bent hawaiian-emperor hotspot track: inheriting the mantle wind. *Science (1979)*. doi:10.1126/science.1161256
Taylor, G., 1950. The instability of liquid surfaces when accelerated in a direction perpendicular to their planes. I. *Proc R Soc Lond A Math Phys Sci*, **201**, 192–196, The Royal Society. doi:10.1098/RSPA.1950.0052
Thieulot, C, 2014. ELEFANT: a user-friendly multipurpose geodynamics code. *Solid Earth Discussions*, **6**, 1949–2096. doi:10.5194/sed-6-1949-2014
Thieulot, Cedric, 2011. FANTOM: Two- and three-dimensional numerical modelling of creeping flows for the solution of geological problems. *Physics of the Earth and Planetary Interiors*, **188**. doi:10.1016/j.pepi.2011.06.011
Thorne, M.S., Garnero, E.J. & Grand, S.P., 2004. Geographic correlation between hot spots and deep mantle lateral shear-wave velocity gradients. *Physics of the Earth and Planetary Interiors*, **146**, 47–63, Elsevier. doi:10.1016/J.PEPI.2003.09.026
Turcotte, D. & Schubert, G., 2002. *Geodynamics*, 2nd ed., Cambridge University Press. doi:https://doi.org/10.1017/CBO9780511807442
Whitehead, J. A., 1986. Buoyancy-driven instabilities of low-viscosity zones as models of magma-rich zones. *J Geophys Res Solid Earth*, **91**, 9303–9314, John Wiley & Sons, Ltd. doi:10.1029/JB091IB09P09303
Whitehead, John A. & Luther, D.S., 1975. Dynamics of laboratory diapir and plume models. *J Geophys Res*, **80**. doi:10.1029/jb080i005p00705

Wilcock, W.S.D. & Whitehead, J.A., 1991. The Rayleigh-Taylor instability of an embedded layer of low-viscosity fluid. *J Geophys Res Solid Earth*, **96**, 12193–12200, John Wiley & Sons, Ltd. doi:10.1029/91JB00339

Zhou, Y., 2017. Rayleigh–Taylor and Richtmyer–Meshkov instability induced flow, turbulence, and mixing. I. *Phys Rep*. doi:10.1016/j.physrep.2017.07.005

Zhou, Y., 2017. Rayleigh–Taylor and Richtmyer–Meshkov instability induced flow, turbulence, and mixing. II. *Phys Rep*. doi:10.1016/j.physrep.2017.07.008

Zhou, Y., Clark, T.T., Clark, D.S., Gail Glendinning, S., Aaron Skinner, M., Huntington, C.M., Hurricane, O.A., *et al.*, 2019. Turbulent mixing and transition criteria of flows induced by hydrodynamic instabilities. *Phys Plasmas*, **26**. doi:10.1063/1.5088745

Zhou, Y., Williams, R.J.R., Ramaprabhu, P., Groom, M., Thornber, B., Hillier, A., Mostert, W., *et al.*, 2021. Rayleigh–Taylor and Richtmyer–Meshkov instabilities: A journey through scales. *Physica D*. doi:10.1016/j.physd.2020.132838

Zrnić, D.S. & Hendricks, C.D., 2003. Stabilization of the Rayleigh-Taylor Instability with Magnetic Feedback. *Phys Fluids*, **13**, 618, American Institute of PhysicsAIP. doi:10.1063/1.1692967

Appendix A:

Benchmark 1: Falling block experiment

This straightforward benchmark test is performed to ensure the applicability of the UNDERWORLD2 code in numerical simulation of a mechanical system consisting of substantial viscosity variations inside the simulation domain. This benchmark test comprises of an isolated square viscous object (ρ_2, μ_2) of higher density that sinks in a low-viscosity medium of lower density (ρ_1, μ_1) under its own weigh. The numerical model domain represents a square with dimensions L_x = L_y = 500 km, where the square (100 km x 100 km) block is initially positioned with its centre at x = 250 km, y = 400 km (see Fig. A1). The simulation is carried out on a 101 x 101 elements grid, each element initially containing 30 x 30 particles. We impose free-slip boundary conditions on all sides of the model domain. The mechanical setting considered in this benchmark test differs from that of a benchmark test for Rayleigh – Taylor instabilities in a two-layer system. In the latter case the model has both the fluid layers extended to the model domain boundaries, whereas one-fluid object (denser in our case) is entirely surrounded by a lighter fluid in the falling block benchmark test.

Our benchmark test results satisfy the following criteria: (i) reducing deformation of the block with increasing viscosity contrast (Fig. A1) and (ii) sinking velocity of the block being independent to its own viscosity at large viscosity ratios (>10^4), as performed in earlier benchmark studies (Thieulot 2011; Gerya 2019). The benchmark experiment thus validates the application of the UNDERWORLD2 code in our study. This benchmark test also demonstrates the accurate conservation properties of the numerical scheme in terms of preserving the block edges' geometry at significant deformation and high viscosity contrasts. These tests are run by varying the block viscosity, keeping the density (ρ_1 = 3200 kg/m^3) and viscosity (10^{21} Pa s) of the ambient medium constant. The details of following five experiments are presented in Fig. A1.

Exp 1: $\rho_2 = 3300$ kg/m^3 , $\mu_2 = 10^{21}$ Pa s

Exp 2: $\rho_2 = 3300$ kg/m^3 , $\mu_2 = 10^{22}$ Pa s

Exp 3: $\rho_2 = 3300$ kg/m^3 , $\mu_2 = 10^{23}$ Pa s

Exp 4: $\rho_2 = 3300$ kg/m^3 , $\mu_2 = 10^{25}$ Pa s

Exp 5: $\rho_2 = 3300$ kg/m^3 , $\mu_2 = 10^{27}$ Pa s

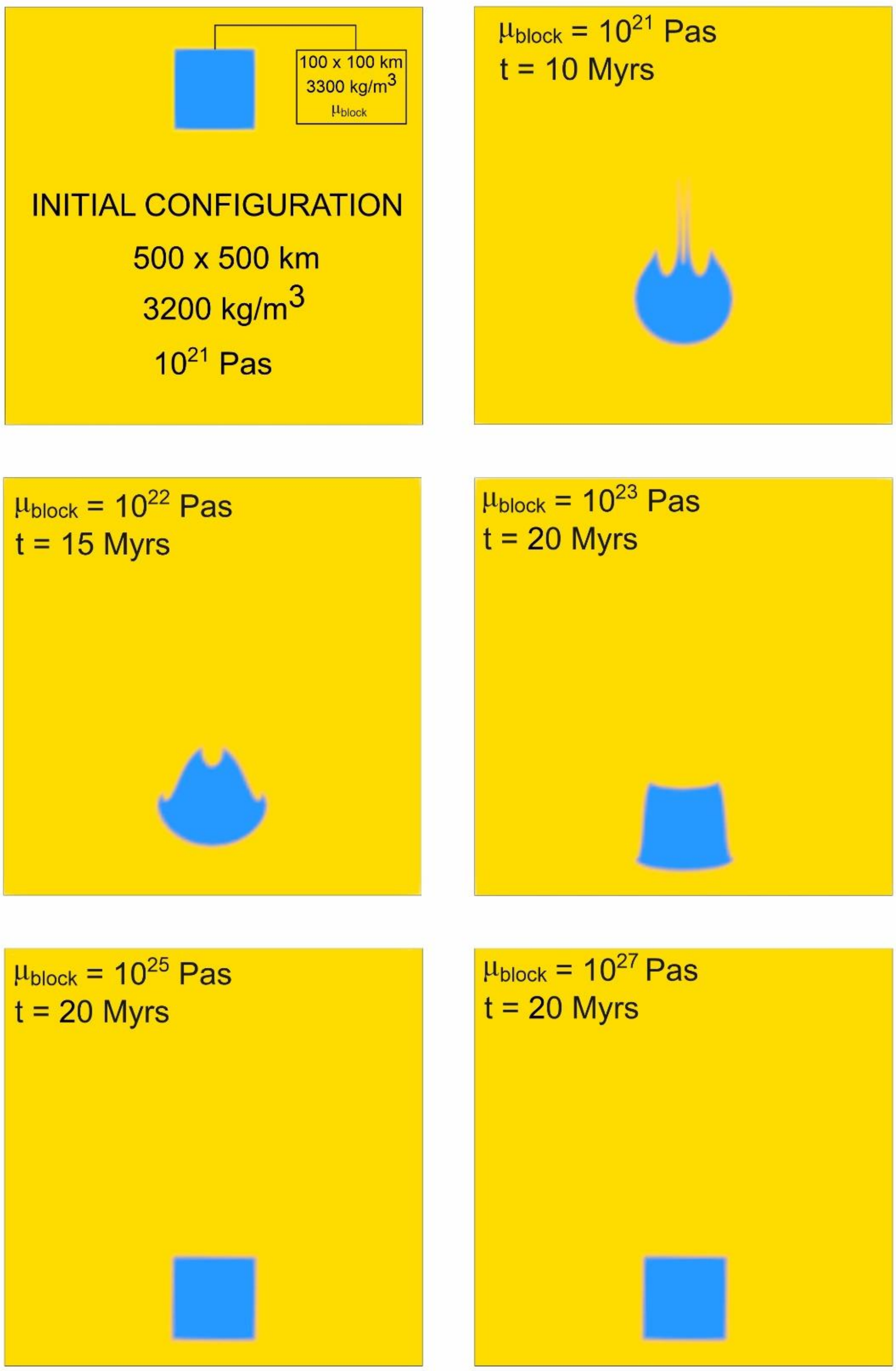

Figure A1: Falling-block benchmark experiments for $\Delta\rho = 100\ kg/m^3$. Initial model conditions are shown in the top left panel. Note that the degree of block deformation decreases with increasing block viscosity (indicated top left corner of each panel, which match well with the previous simulation results (Gerya, 2010; Thieulot, 2011)

From experiments the block velocity is plotted as a function of the viscosity ratio ($\log \frac{\mu_{block}}{\mu_{medium}}$) (Fig. A2). The experimental data follow a well-defined characteristic curve, which further allows us to confirm that the UNDERWORLD2 code can accurately capture gravity driven motion of any object within a medium characterized by significant viscosity variations.

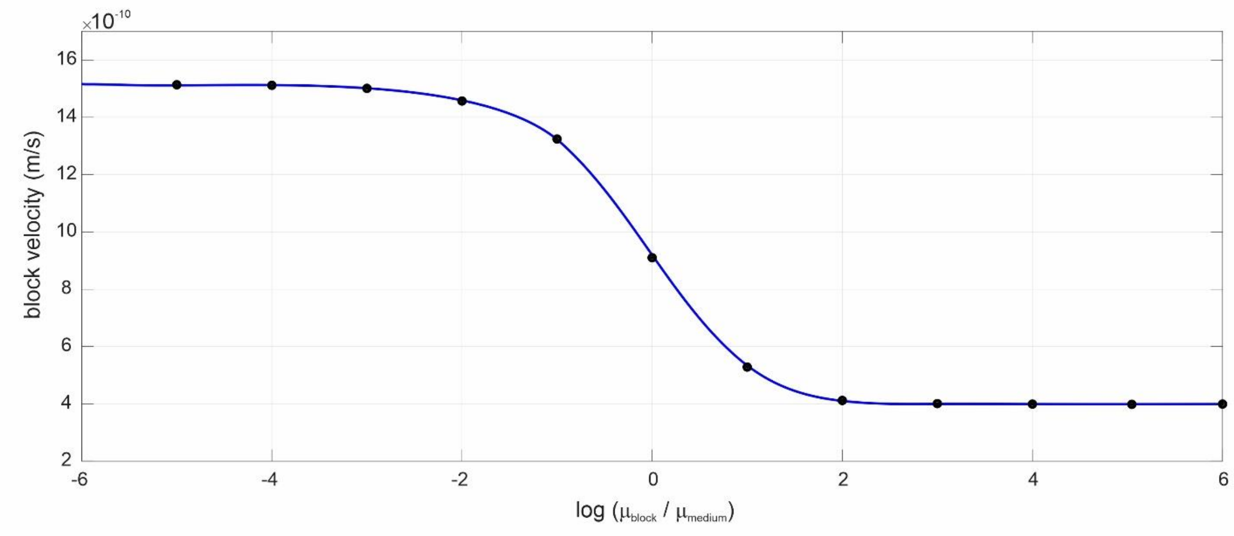

Figure A2: Calculated plot of the block-sinking velocity as a function of the block to host viscosity ratio ($\log \frac{\mu_{block}}{\mu_{medium}}$). This characteristic geometry of the curve is consistent with the available data (details in the text).

Benchmark 2: van Keken et al (1997) numerical experiment

This benchmark aims to reproduce the results of van Keken et al (1997), who validated numerical experiments on the Rayleigh-Taylor instability phenomenon in a two-layer fluid system with inverted density stratification (Fig. A3). Several other authors have also benchmarked this numerical problem using various techniques, such as tracers (Tackley & King 2003), level set method (Hillebrand *et al.* 2014), particle level set method (Samuel & Evonuk 2010), and face-centred finite volume (Burcet *et al.* 2023). Our benchmark experiment uses a square model domain of height $L_y = 1$ and width L_x= 0.9142, containing a lighter viscous layer with density ρ_2 and viscosity μ_2, overlain by a denser layer of density $\rho_1$and

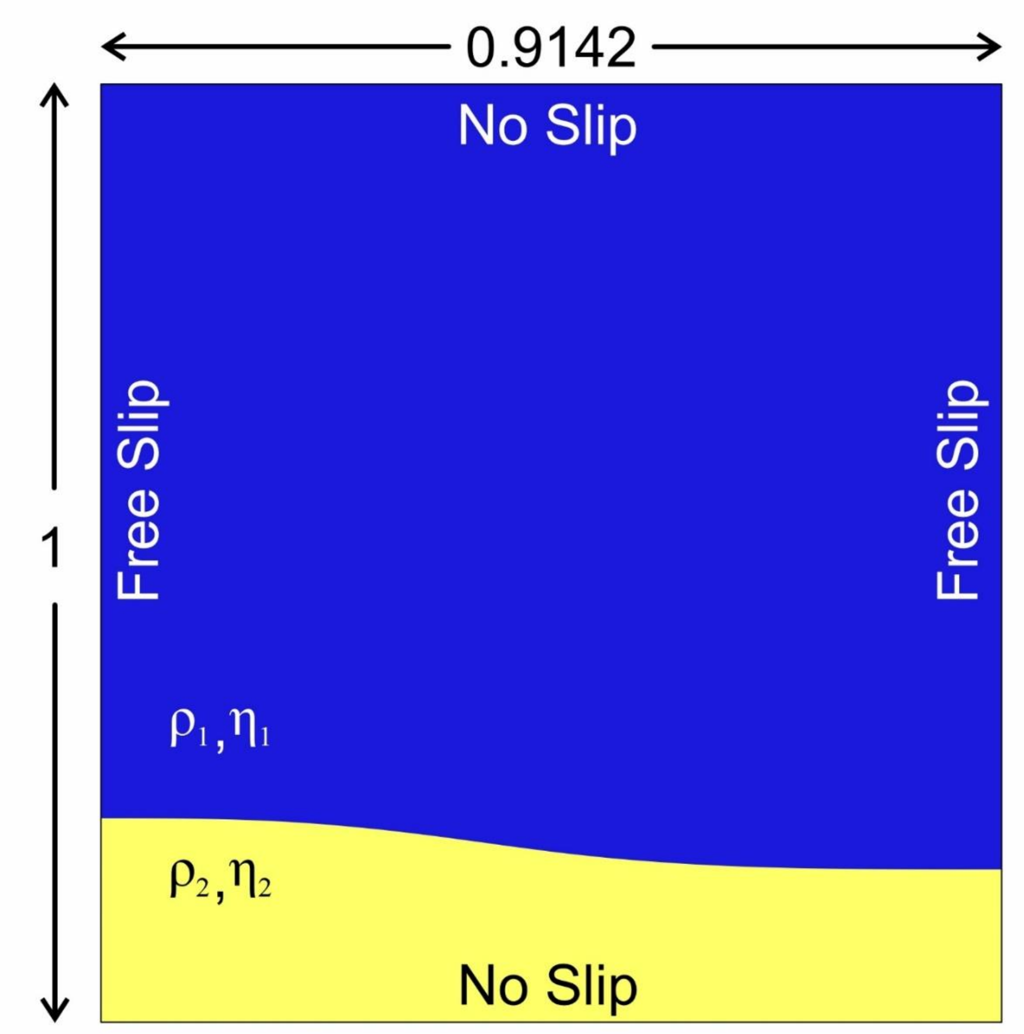

Figure A3: Initial model set-up and boundary conditions used for the Van Keken benchmark test.

viscosity μ_1. The initial geometrical perturbation at their interface is imposed in the form of waves as,

$$y(x) = 0.2 + 0.02cos\left(\frac{\pi x}{\lambda}\right), \tag{A2.1}$$

where λ (= 0.9142) denotes the wavelength of perturbations. The bottom lighter fluid is assigned density ρ_2 = 1000 and viscosity μ_2 = 100, and the density of the top heavier layer ρ_1 = 1010, keeping μ_1 = μ_2 . No-slip conditions are applied at the bottom and top boundaries of the box, whereas free-slip boundary conditions are imposed on both the lateral sides. In this benchmark study, we take snapshots of the material field at regular intervals, and compare the corresponding results with those of van Keken et al., 1997. We also compare the evolution of the root mean square velocity (v_{rms}) of the entire domain over time, specifically concentrating on the timing and the corresponding height of the first peak, which coincides with the rise of the first diapir. The v_{rms} of the system is given by,

$$v_{rms} = \sqrt{\frac{1}{V} \int \|v\|^2 \, dV}, \tag{A2.2}$$

where *V* is the domain volume.

Method (Code)	Grid	Time	v_{rms} (max)	Source
Tracers (ELEFANT)	400x400	208.7	0.003093	Thieulot (2014)
Marker Chain	30x30	213.38	0.00300	PvK in Van Keken et al. (1997)
	50x50	211.81	0.003016	
	80x80	210.75	0.003050	
Particle-in-cell FEM	32x32	227.53	0.003144	This Study
	128x128	214.124	0.003120	
	256x256	211.165	0.003107	
	512x512	210.165	0.003102	

Table A1: Comparison of v_{rms} – model run time values obtained from different numerical methods.

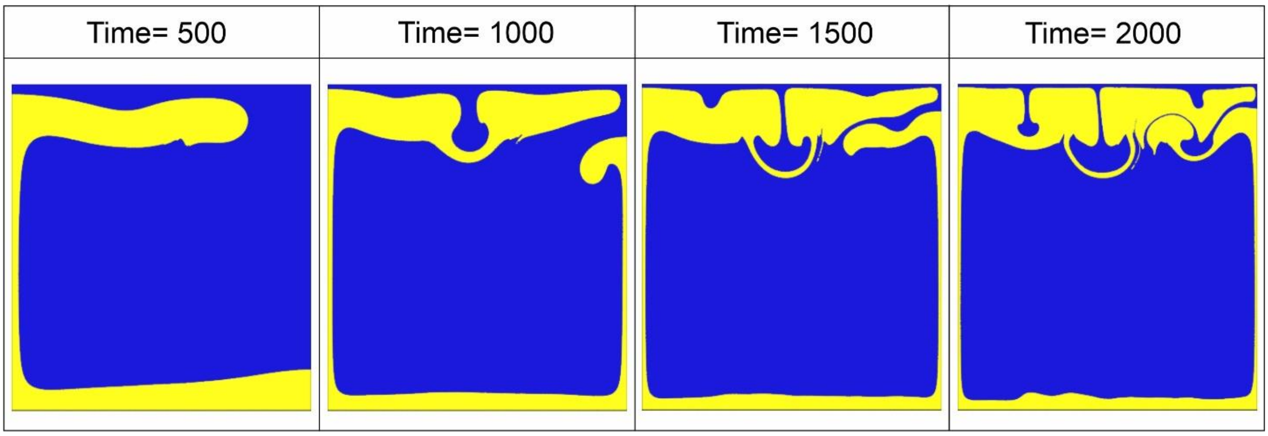

Figure A4: Time-series simulations of the Rayleigh-Taylor instabilities in the van Keken benchmark test with viscosity ratio = 1 (model run time indicated at the top of each panel).

The temporal evolution of the benchmark experiments is shown in Fig A4. The long-wavelength perturbation on the initial interface (Eq. A2.1) selectively grows and determines the rise of the first plume along the left edge of the domain (Fig. A4), followed by the rise of a second plume on the right edge. The fluid interface at t = 2000, shown in Fig.A4 visually matches with that in figure 2 of van Keken et al. (1997). Table A1 shows the comparison between v_{rms}/time values for different numerical methods. Fig. A5 presents the v_{rms} measurements for a 512 × 512 grids simulation, providing a comparison with those of van Keken et al. (1997). It is to note that our calculated curves match well in terms of the position and height of the peaks with theirs.

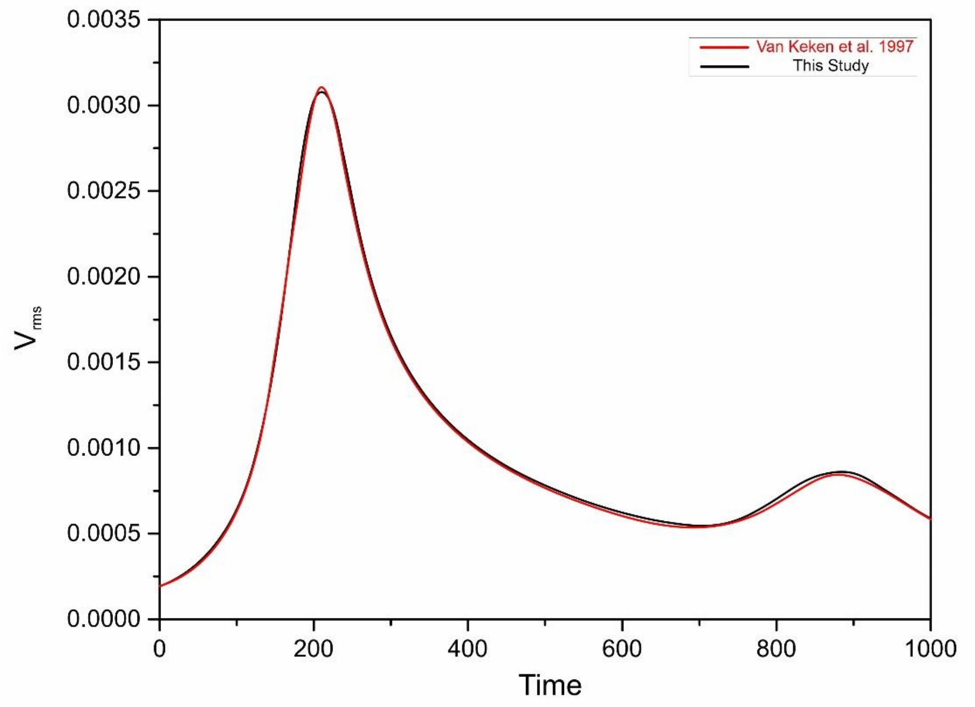

Figure A5: Graphical plot of the root mean square velocity (v_{rms}) as a function of time from the present van Keken benchmark test results (black) and the earlier plot (red line) given by van Keken et al., (1997) PvK (Marker chain) numerical method.

Benchmark 3: Rayleigh-Taylor instability experiment

This benchmark is based on the analytical solution by Ramberg (1968), which is extensively used in numerical modelling (Gerya 2009; Thieulot 2011). The numerical model setup consists of an initial sinusoidal wave of geometrical perturbation with a small initial amplitude ΔA and a wavelength $\lambda = \frac{L_x}{2}$ at the boundary between the two layers (upper: μ_1, ρ_1) and lower: μ_2, ρ_2) of thicknesses h_1 and h_2, respectively. A no-slip boundary condition is imposed at the top and the bottom of the box, while a free-slip condition on the lateral side walls. We choose ρ_1= 3300 kg/m^3, ρ_2 = 3300 kg/m^3, μ_1 = 10^{21} Pa s, 10^{19} Pa s < μ_2< 10^{27} Pa s, $h_1 + h_2 = L_y$ = 500 km in our model simulations, similar to those used in Thieulot (2011).

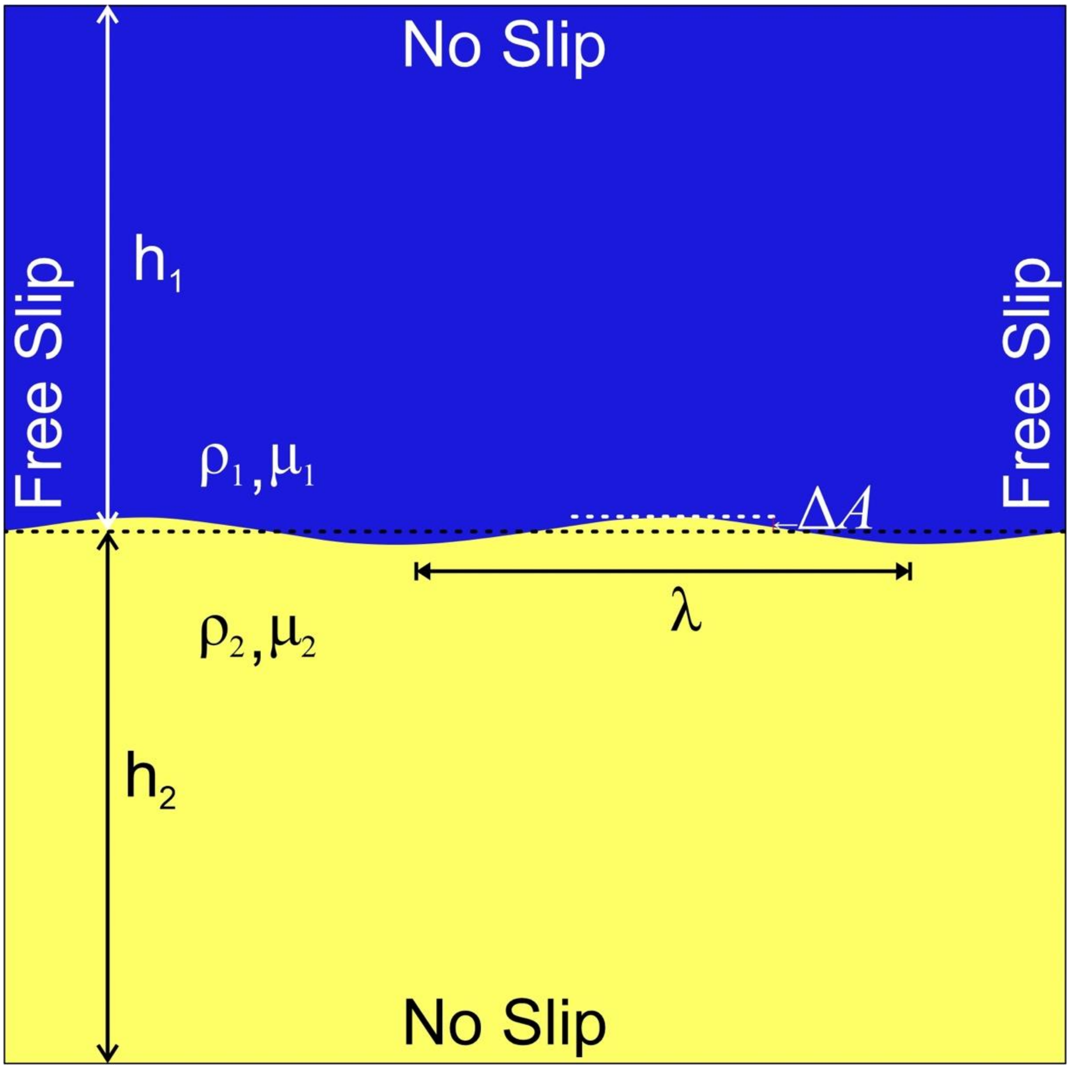

Figure A6: Initial model configuration and boundary conditions chosen for the Rayleigh-Taylor Instability benchmark test.

After Ramberg's solution, the velocity of diapiric growth, v_y follows,

$$\frac{v_y}{\Delta A} = -K \frac{\rho_1 - \rho_2}{2\mu_2} h_2 g \,, \qquad \text{(A38)}$$

where the non-dimensional growth factor $K = -\frac{a_{12}}{b_{11} j_{22} - a_{12} i_{21}}$, and

$$\omega_1 = \frac{2\pi h_1}{\lambda} \,, \qquad \omega_2 = \frac{2\pi h_2}{\lambda},$$

$$b_{11} = \frac{\mu_1 2{\omega_1}^2}{\mu_2 \, (cosh\, 2\omega_1 - 1 - 2{\omega_1}^2)} - \frac{2{\omega_2}^2}{cosh\, 2\omega_2 - 1 - 2{\omega_2}^2},$$

$$a_{12} = \frac{\mu_1(\sinh 2\omega_1 - 2\omega_1)}{\mu_2 \, (cosh\, 2\omega_1 - 1 - 2{\omega_1}^2)} - \frac{\sinh 2\omega_2 - 2\omega_2}{cosh\, 2\omega_2 - 1 - 2{\omega_2}^2},$$

$$i_{21} = \frac{\mu_1 \omega_2(\sinh 2\omega_1 - 2\omega_1)}{\mu_2 \, (cosh\, 2\omega_1 - 1 - 2{\omega_1}^2)} + \frac{\omega_2(\sinh 2\omega_2 + 2\omega_2)}{cosh\, 2\omega_2 - 1 - 2{\omega_2}^2},$$

$$j_{22} = \frac{\mu_1 2{\omega_1}^2 \omega_2}{\mu_2(cosh\, 2\omega_1 - 1 - 2{\omega_1}^2)} + \frac{2{\omega_2}^3}{cosh\, 2\omega_2 - 1 - 2{\omega_2}^2},$$

L_x is varied between 500 and 1500 km, leading to $\frac{2\pi}{3} \leq \omega_1 \leq 2\pi$. g is the acceleration due to gravity.

Our benchmark test was run with a constant resolution of 75 x 75 elements for all the simulations. We performed two sets of measurements considering the perturbation amplitude: 1) $\Delta A = s_y$ and 2) $\Delta A = \frac{s_y}{3}$, where s_y (=s_x) is the size of an element. The results are presented in Fig. A7, which clearly reveals that, over a wide range of the viscosity ratio, our model estimates agree well with the values obtained from the analytical solution (Eq. A3.1). This match validates our application of the UNDERWORLD2 code to model the velocity fields of gravity driven flows in a system with sharp and strong viscosity variations.

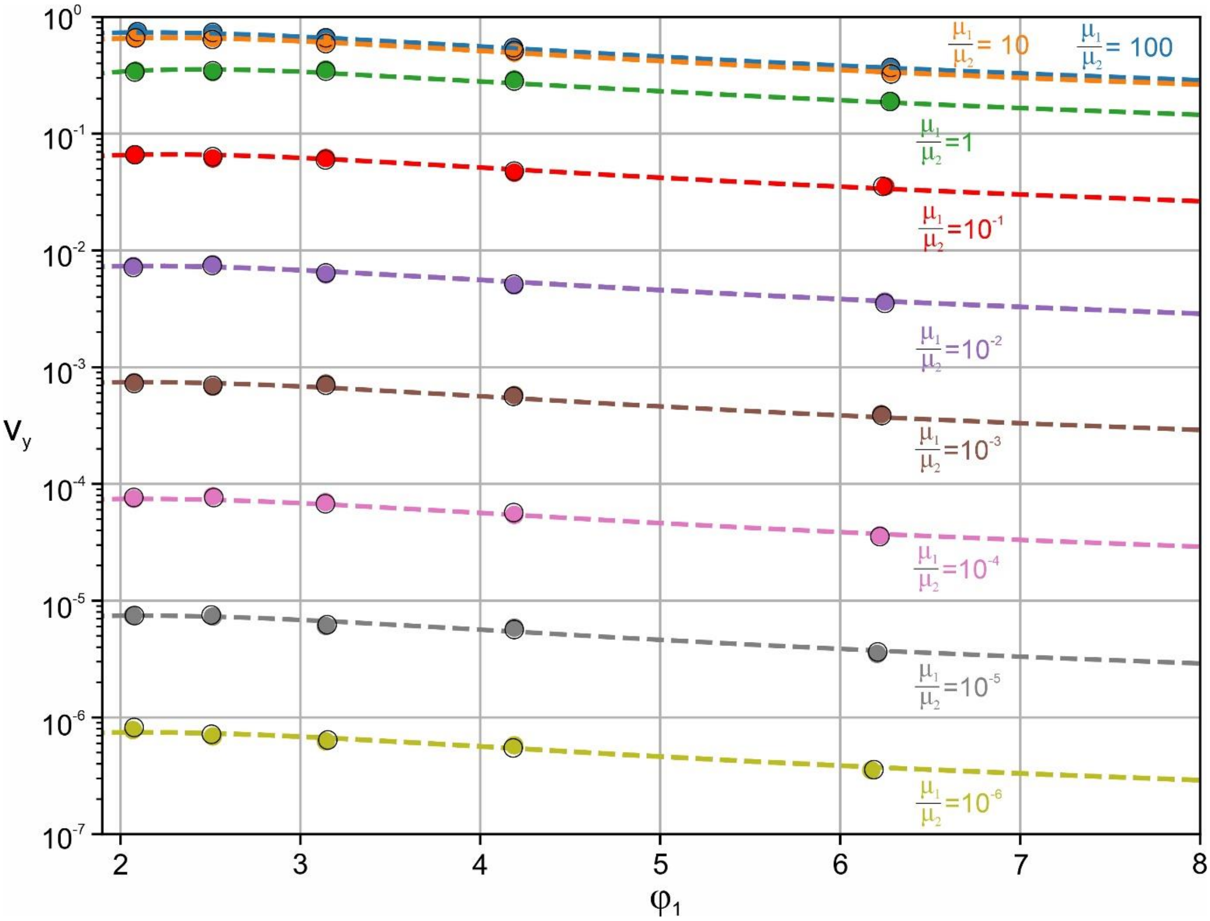

Figure A7: Benchmark test results (symbols) for two different initial amplitudes: ΔA = s_y and $\frac{s_y}{3}$. Dashed lines represent Ramberg's analytical solutions.

Figure 1:

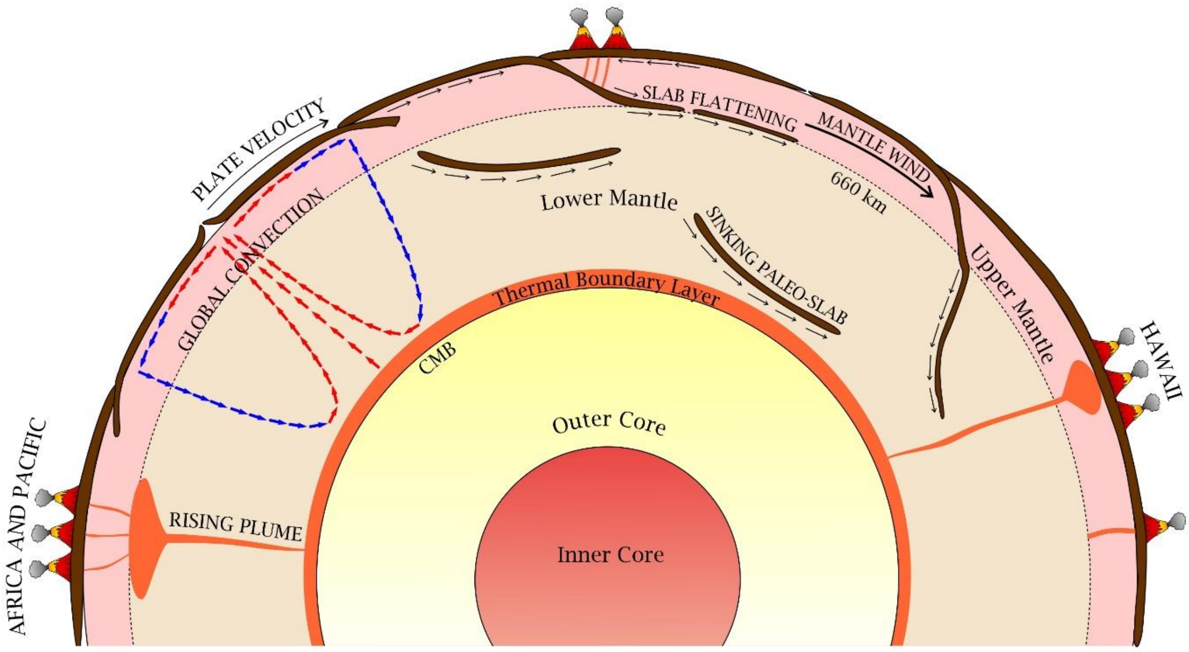

Figure 1: Schematic presentation of the Earth's interior showing major locations of plume generation in the mantle and associated volcanisms on the surface. Different types of mantle flows, such as convection-, sinking slab-, lithospheric plate-driven flows and mantle wind are also depicted. All deep-source plumes, forming hotspots, like the Hawaiian chain, originate from the thermal boundary layer (TBL) at the core-mantle boundary (CMB).

Figure 2:

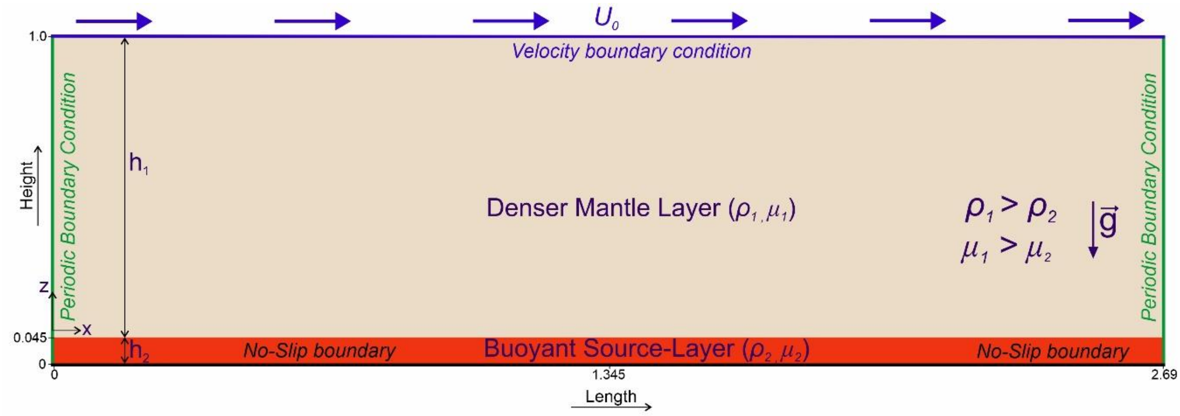

Figure 2: Initial CFD model set-up and associated boundary conditions used for simulations of Rayleigh-Taylor instabilities in the lower mantle domain. Denser (ρ_1) overburden layer overlies a thin lighter (ρ_2) basal layer (source layer). The model domain is discretized into elements with a mesh resolution of 1024 x 512. The side and the bottom walls are assigned periodic and no-slip boundary conditions, respectively. The top model boundary is imposed with a uniform horizontal velocity, which induces an initial global horizontal flow condition in the overlying denser mantle. **g** is the acceleration due to gravity.

Figure 3:

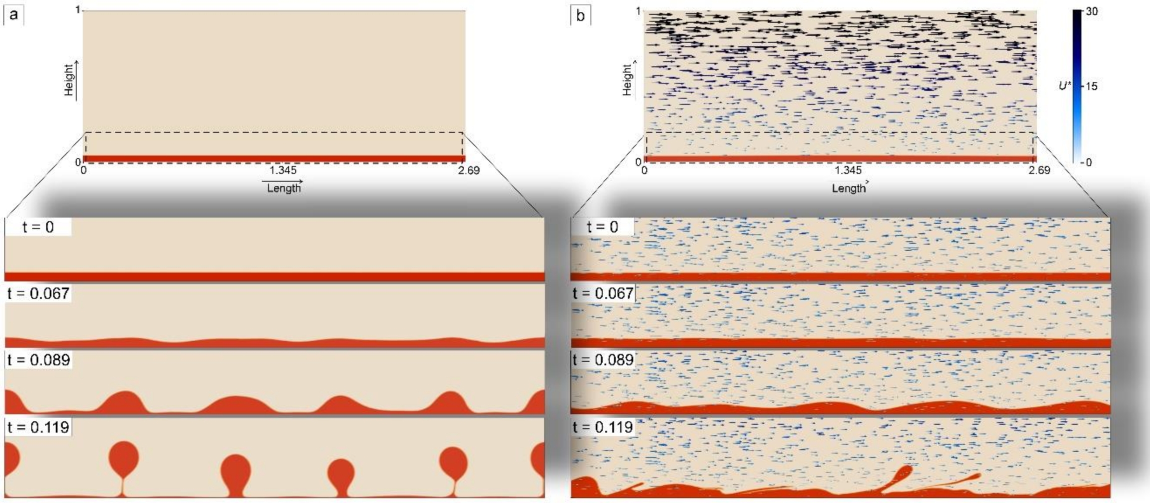

Figure 3: Progressive growth of Rayleigh-Taylor instabilities in CFD model simulations. a) Reference experiment with an initially rest mantle condition ($U^{*}= 0$). b) Experiment with an initial horizontal global flow ($U^{*}=36$) in the mantle. Notice in panel (b) at t = 0.119 that the instability growth is significantly dampened by the global mantle flow. The colour bar represents normalized flow velocity magnitudes.

Figure 4:

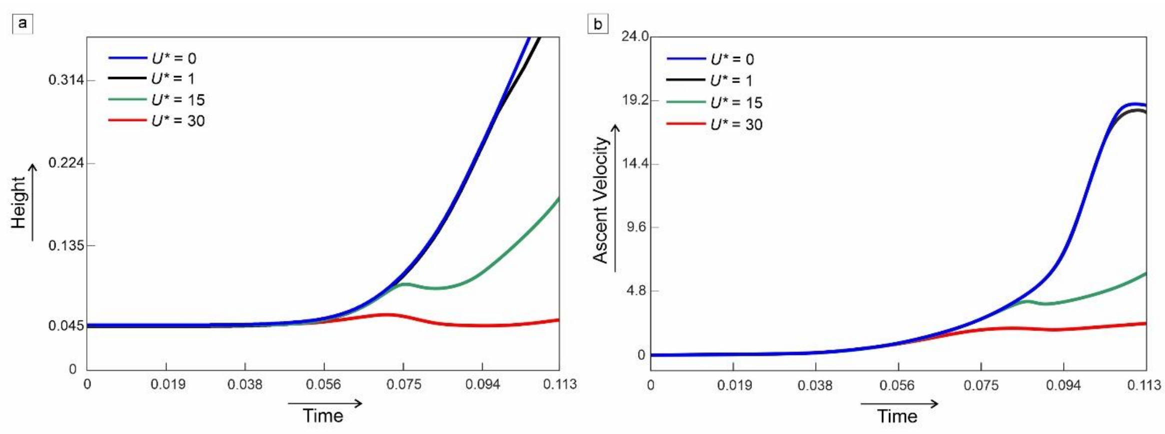

Figure 4: Graphical plots of a) plume ascent heights, and b) vertical ascent velocities of the fastest growing instabilities as a function of time for different normalized global flow-velocity magnitudes (U^*). For this set of simulations, A_T = 0.02 and μ^* = 10^2 .Note that increasing U^* strongly influences the ascent heights and velocities at t > 0.06.

Figure 5:

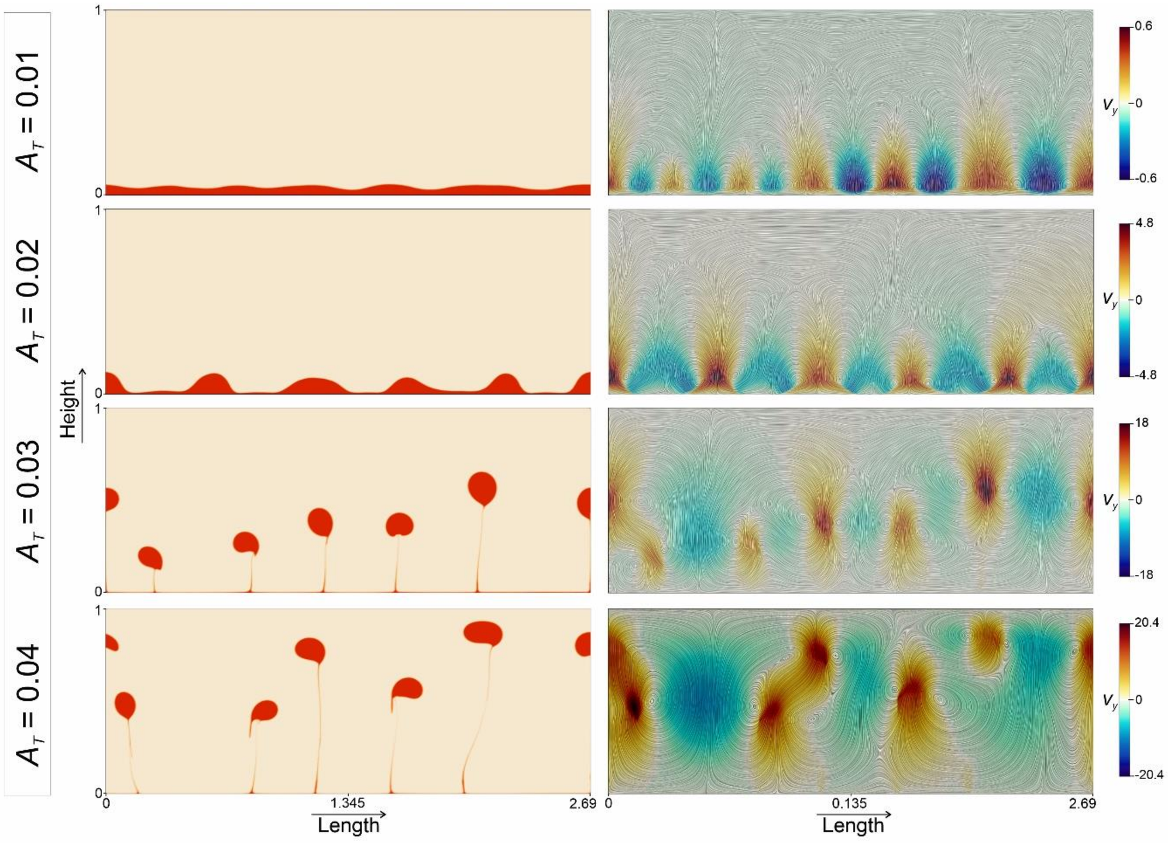

Figure 5: CFD simulations showing the effects of buoyancy factor (A_T) on a) Rayleigh-Taylor instability growth in the buoyant source layers (red colour) and b) the corresponding flow fields represented by streamlines. The colour contours depict the magnitudes of vertical velocity components. The snapshots of four different simulations presented in the row-wise panels correspond to a simulation time of 0.083.

Figure 6:

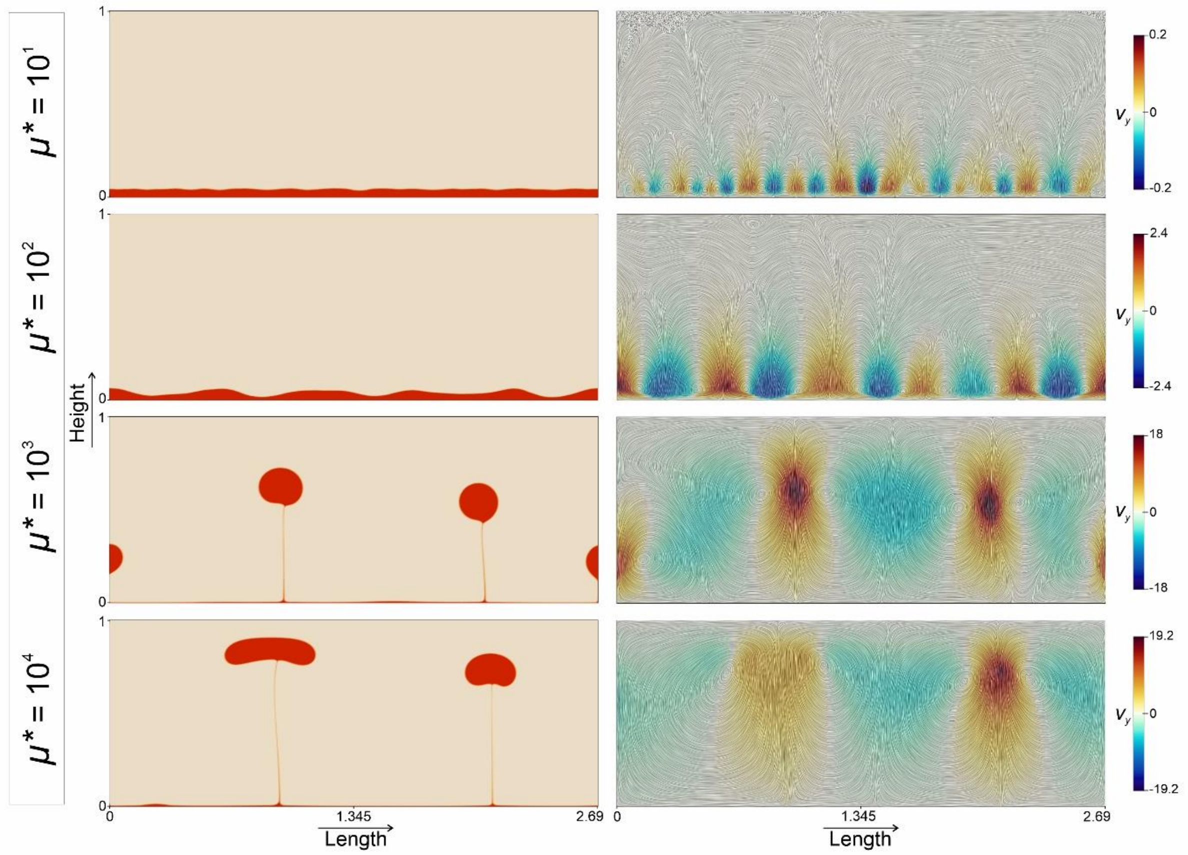

Figure 6: Effects of overburden- to source-layer viscosity μ^* on a) Rayleigh-Taylor instability growth and b) the corresponding flow fields in CFD models. The colour contours depict the magnitudes of vertical velocity components. The snapshots of four different simulations presented in the row-wise panels correspond to a simulation time of 0.075.

Figure 7:

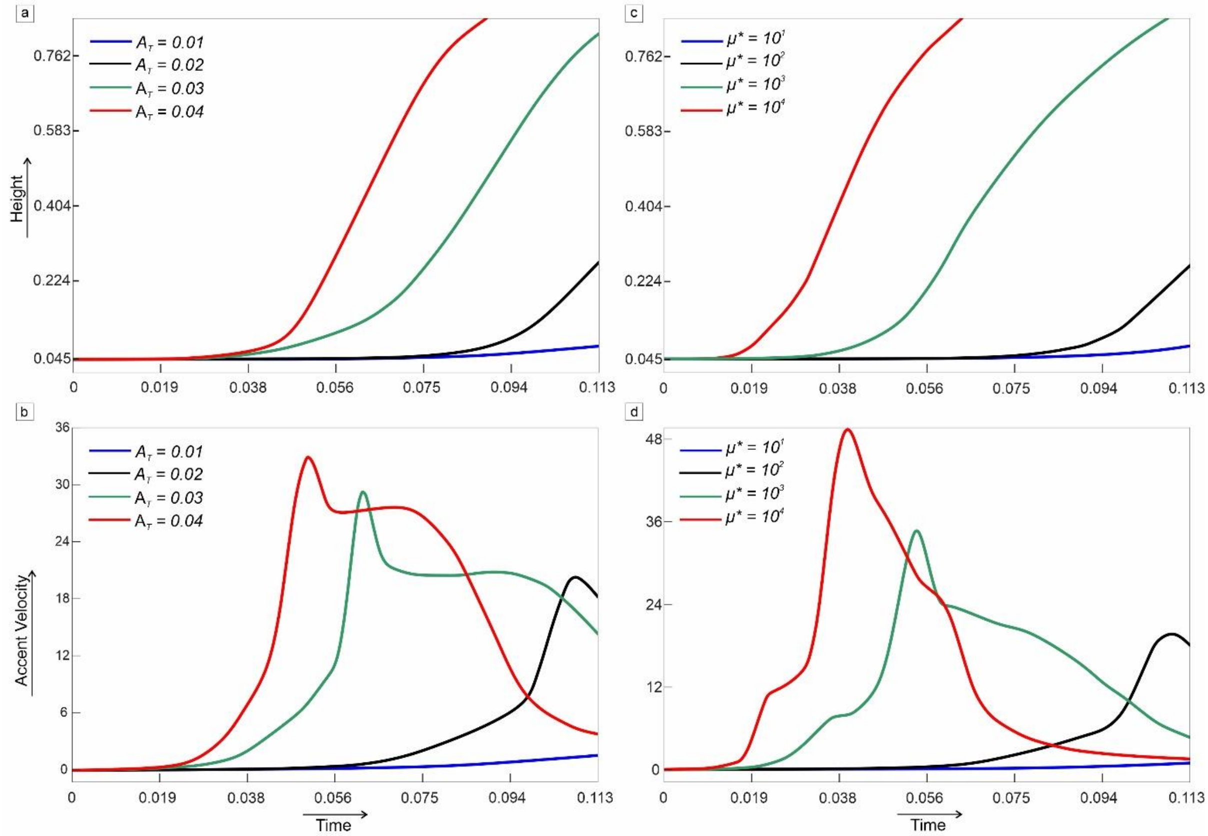

Figure 7: Time series analyses of the plume ascent heights and the vertical ascent velocities of the fastest growing instabilities for different A_T values, keeping $\mu^* = 10^2$ in a) and b), and μ^* values, keeping $A_T = 0.02$ in c) and d), respectively.

Figure 8:

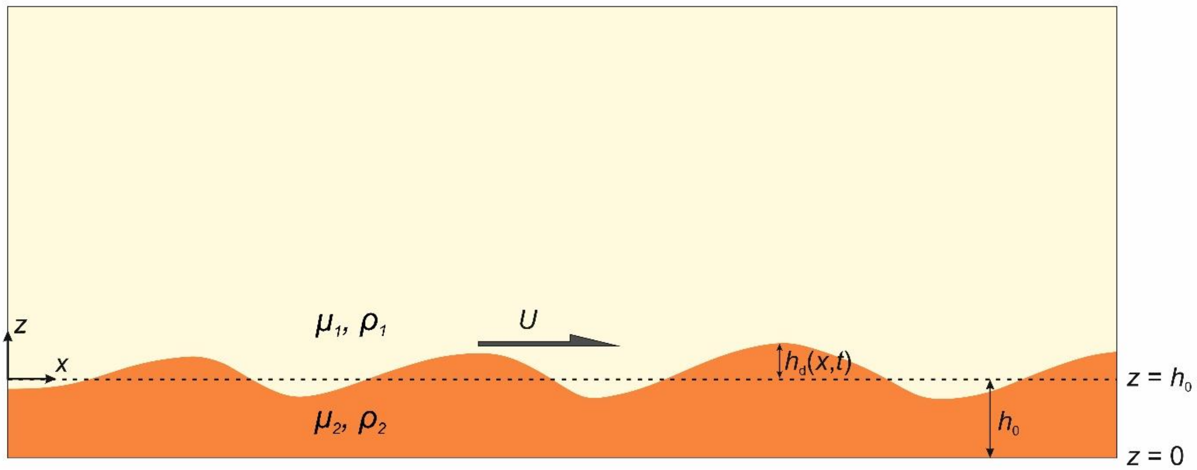

Figure 8: Two-layer fluid system chosen for the linear stability analysis: a thin buoyant layer (source layer) (density: ρ_2 and viscosity: μ_2) underlying a denser fluid layer (density: ρ_1 and viscosity: μ_1) (ambient mantle). Dashed and solid lines denote the initial source-layer configuration and the deformed interface geometry formed by RTI. h_o and h_d define the initial source-layer thickness and the vertical deflection at the interface, respectively. $U_i(x,t)$ represents the horizontal flow velocity at the interface.

Figure 9:

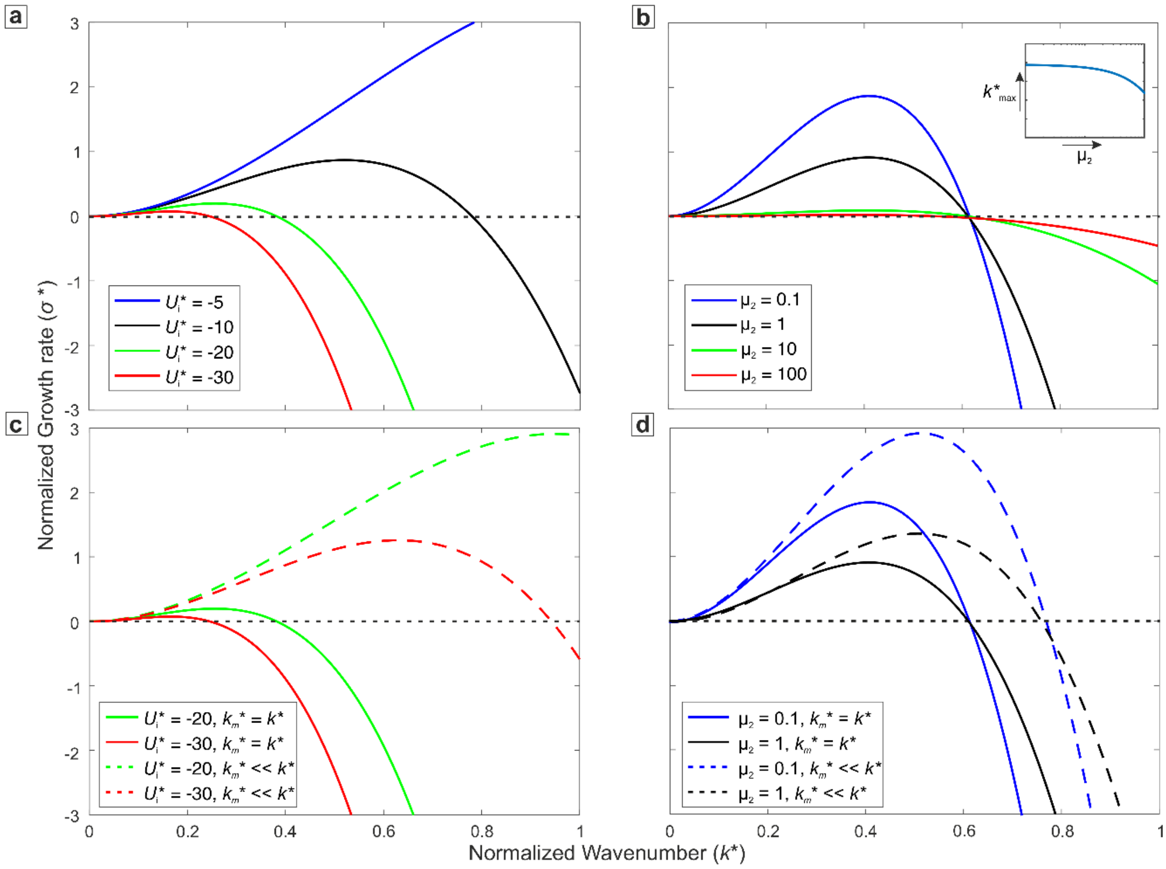

Figure 9: Normalized growth rates σ^* versus normalized wavenumber k^* plots for different values of (a) the ambient mantle velocity U_i^*, and (b) the source layer viscosity μ_2, normalized to overburden viscosity μ_1 obtained from the linear stability analysis for $x^* = 0$ (decreasing wavenumber, i.e. increasing wavelength with μ_2 depicted in the inset). Normalized growth rates σ^* versus normalized wavenumber k^* plots for different values of (c) ambient mantle velocity (U_i^*), and (d) source layer viscosity μ_2 obtained from the linear stability analysis under the condition of $k_M^* = k^*$ and $k_M^* \ll k^*$.

Figure 10:

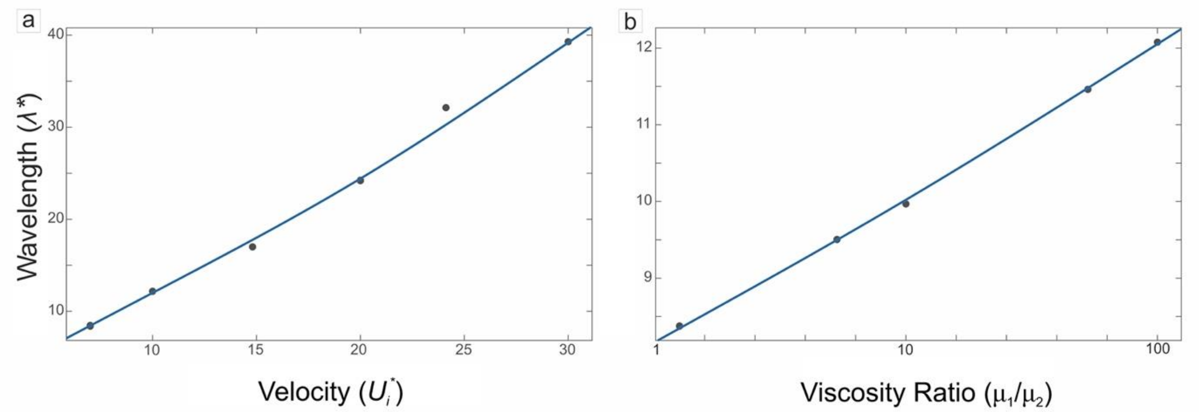

Figure 10: Variations of the instability wavelength (λ^*) with (a) global flow velocity (${U_i}^*$), and (b) mantle-source layer viscosity ratio ($\frac{\mu_1}{\mu_2}$) from the linear stability analysis. All the variables are presented as non-dimensional quantities.

Figure 11:

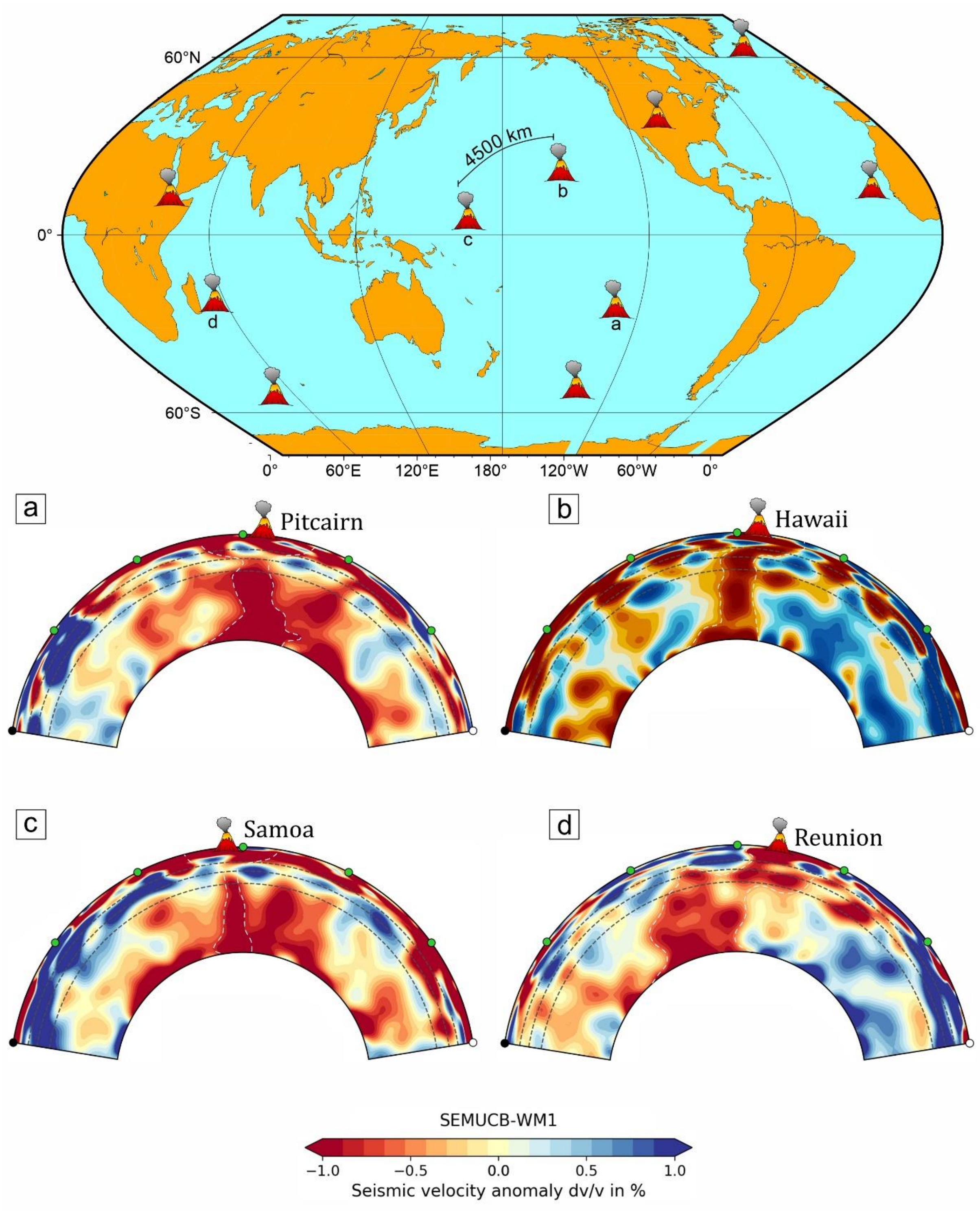

Figure 11: Global distribution of the major hotspots originating from deep-mantle plume sources. The seismic sections (lower panels) show the plume configurations in mantle beneath a) Pitcairn, b) Hawaii, c) Samoa, and d) Afar hotspots. Note that inter-hotspot distances are several thousand kilometres.

Table1: List of physical variables and their corresponding symbols used in this study.

Physical Variable	**Symbol**
Source-layer thickness	h_2
Overburden-layer thickness	h_1
Interfacial deflection	h_d
Mean height of the interface	h_0
Normalized source-layer thickness	h^*
Characteristic $\boldsymbol{x}-$ length scale	L
x- and z- component of velocity in the thin layer	u, v
Excess hydrostatic pressure	p
Density of thin-layer	ρ_2
Density of Mantle	ρ_1
Density contrast	$\Delta\rho = (\rho_1 - \rho_2)$
Viscosity of thin-layer	μ_2
Viscosity of Mantle	μ_1
Horizontal velocity at the interface	U
Maximum horizontal flow at the interface	U_i
Normalized maximum horizontal flow at the interface	U_i^*
Strain rate	$\dot{\epsilon}$
Wavenumber of wave function	k_M
Wavenumber of perturbation	k
Angular frequency	ω
Growth rate	σ
Normalized growth rate	σ^*
Atwood Number	A_T
Total Pressure	P
Initial depth of the interface	D_o
Wavelength of initial perturbation	λ
Initial perturbation amplitude	ΔA
Top model-boundary velocity	U_0
Normalised top model-boundary velocity	U_0^*

Supplementary Information for

Dampening effect of global flows on Rayleigh-Taylor instabilities: Implications for deep-mantle plume vis-à-vis hotspot distributions

Arnab Roy, Dip Ghosh and Nibir Mandal
Department of Geological Sciences, Jadavpur University, Kolkata 700032, India

S1. Choice of the bottom boundary conditions in numerical modelling

The boundary conditions imposed at the model base is a crucially important consideration to model a mechanical system. No-slip and free-slip are the two most common types of boundary conditions used to constrain the bottom boundary setting of a model. Our numerical modelling introduces a no-slip boundary condition to ensure a coherent interface of the source layer with the substrate, allowing no movement at its bottom boundary. Consequently, the source layer, in overall, is held fixed to the base although it undergoes internal flows with the overburden fluid. The no-slip boundary condition enables us to set a relative horizontal global flow between the source layer and its overburden, which is the main concern of the present study. It is noteworthy that this relative kinematics in the two-layer system could not be achieved if a free-slip condition were chosen at the bottom wall. Such a boundary condition would cause both the layers to translate in the horizontal direction, setting little or no relative velocity in the horizontal direction. We thus chose a no-slip bottom boundary condition to obtain the maximum effect of the global mantle flow on plume growth in the source layer.

S2. Mesh-Resolution Tests

The mesh resolution for all the models presented in the main text is 1024×512. We, however, performed mesh resolution tests on a wide spectrum, varying from low resolutions (256×128, 384×384, 512×384, 512×512, 784×512) to an extremely high resolution (2048×1024 elements). The numerical domain covers a normalized length of 2.69 and a normalized height of 1 in the horizontal and vertical directions, respectively. The resolution tests indicate that a mesh resolution of 1024×512 provides optimum refinement in modelling the Rayleigh-Taylor instabilities in the buoyant basal layer.

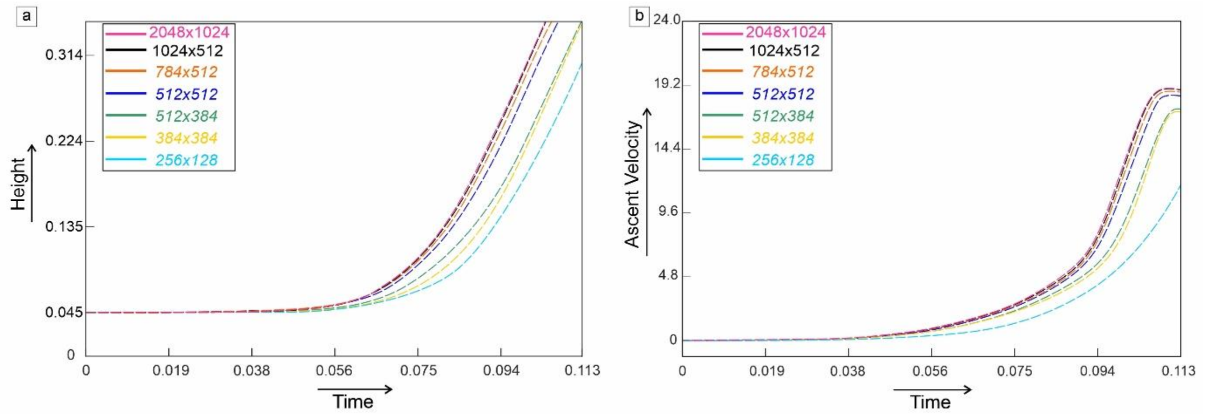

Figure S2: Graphical plots of a) plume ascent heights, and b) vertical ascent velocities of the fastest growing instabilities as a function of time for different mesh resolution.

S3. Normalization of plume growth velocity

We used Ramberg's (1968) analytical solution to normalize plume growth velocity (v_y) calculated from our CFD models in the following way. Consider an initial sinusoidal perturbation with a small initial amplitude (ΔA) and a wavelength (λ) at the interface between the two layers: upper (μ_1, ρ_1) and lower (μ_2, ρ_2) of thicknesses h_1 and h_2, respectively. For the present problem, $\rho_1 > \rho_2$ and $\mu_1 > \mu_2$ and g is the acceleration due to gravity. After Ramberg's solution, the velocity of diapiric growth (v_y) is expressed as,

$$\frac{v_y}{\Delta A} = -K \frac{\rho_1 - \rho_2}{2\mu_2} h_2 g \,, \qquad \text{(S1)}$$

where the non-dimensional factor, $K = -\frac{a_{12}}{b_{11} j_{22} - a_{12} i_{21}}$, and

$$\omega_1 = \frac{2\pi h_1}{\lambda} \,, \; \omega_2 = \frac{2\pi h_2}{\lambda},$$

$$b_{11} = \frac{\mu_1 2\omega_1{}^2}{\mu_2\,(cosh\,2\omega_1 - 1 - 2\omega_1{}^2)} - \frac{2\omega_2{}^2}{cosh\,2\omega_2 - 1 - 2\omega_2{}^2},$$

$$a_{12} = \frac{\mu_1(\sinh 2\omega_1 - 2\omega_1)}{\mu_2\,(cosh\,2\omega_1 - 1 - 2\omega_1{}^2)} - \frac{\sinh 2\omega_2 - 2\omega_2}{cosh\,2\omega_2 - 1 - 2\omega_2{}^2},$$

$$i_{21} = \frac{\mu_1 \omega_2 (\sinh 2\omega_1 - 2\omega_1)}{\mu_2\, (cosh\, 2\omega_1 - 1 - \, 2{\omega_1}^2)} \;\; + \frac{\omega_2 (\sinh 2\omega_2 + 2\omega_2)}{cosh\, 2\omega_2 \; - \; 1 \; - \; 2{\omega_2}^2},$$

$$j_{22} = \frac{\mu_1 2{\omega_1}^2 \omega_2}{\mu_2 (cosh\, 2\omega_1 - 1 - \, 2{\omega_1}^2)} \;\; + \frac{2{\omega_2}^3}{cosh\, 2\omega_2 \; - \; 1 \; - \; 2{\omega_2}^2},$$

S4. CFD simulation with horizontal mantle flow (U^*=18):

We systematically increased the top model-boundary velocity (U_o) to evaluate the effect of global flows on the growth rates of instabilities in the source layer. The non-dimensional boundary velocity, $U^* = U_o \,/\, v_y$ was assigned a value of 18, keeping A_T and μ^* constant.

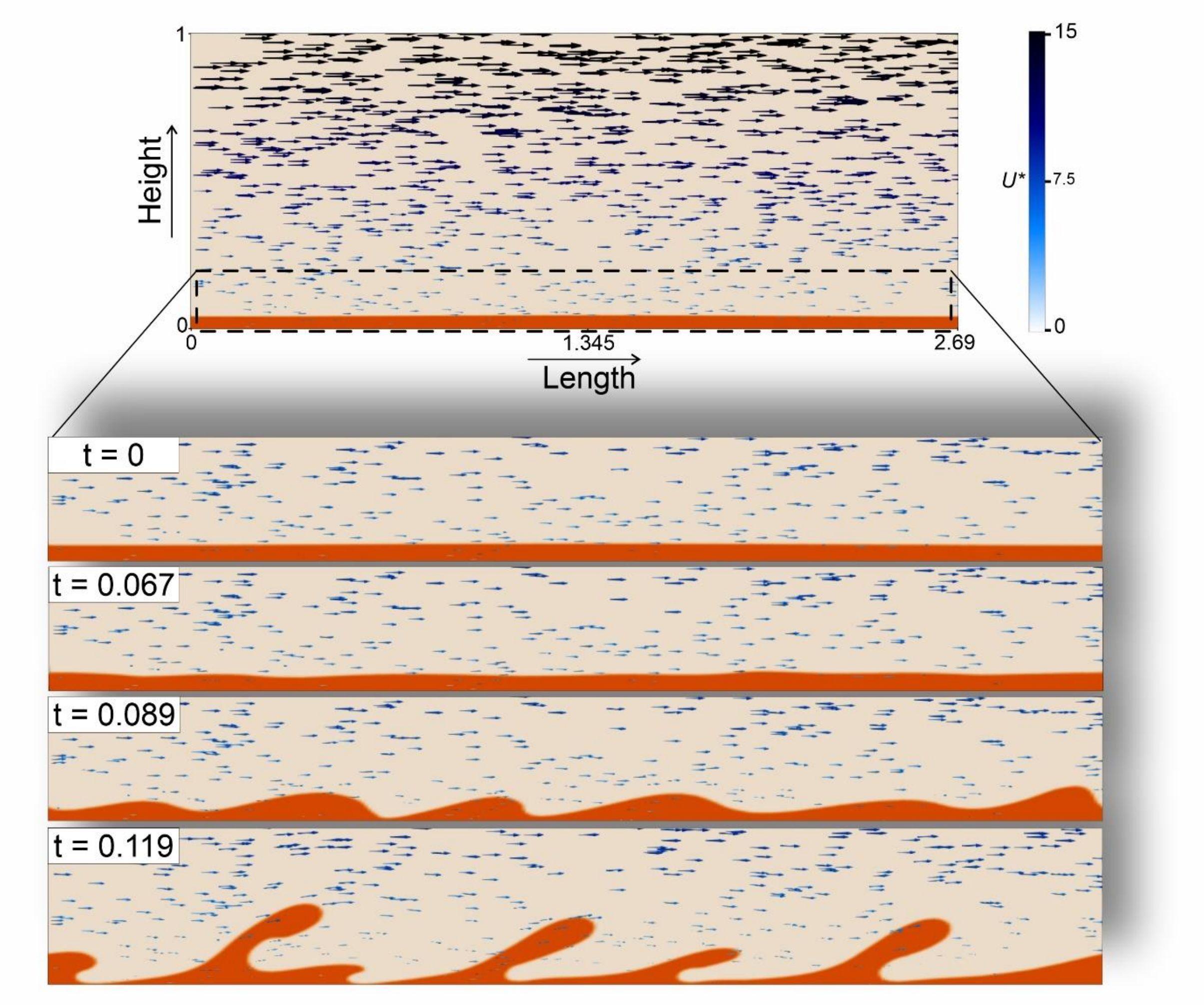

Figure S4: Progressive growth of Rayleigh-Taylor instabilities in CFD model simulations with an initial horizontal global flow (U^*=18) in the mantle.

S5. CFD simulations with varying Atwood Number (A_T) and viscosity ratio (μ^*)

This section present CFD simulation results to show the evolution of Rayleigh-Taylor instabilities as function of A_T (0.01- 0.04) and μ^* (10^1- 10^4) (Figs. S5a-d).

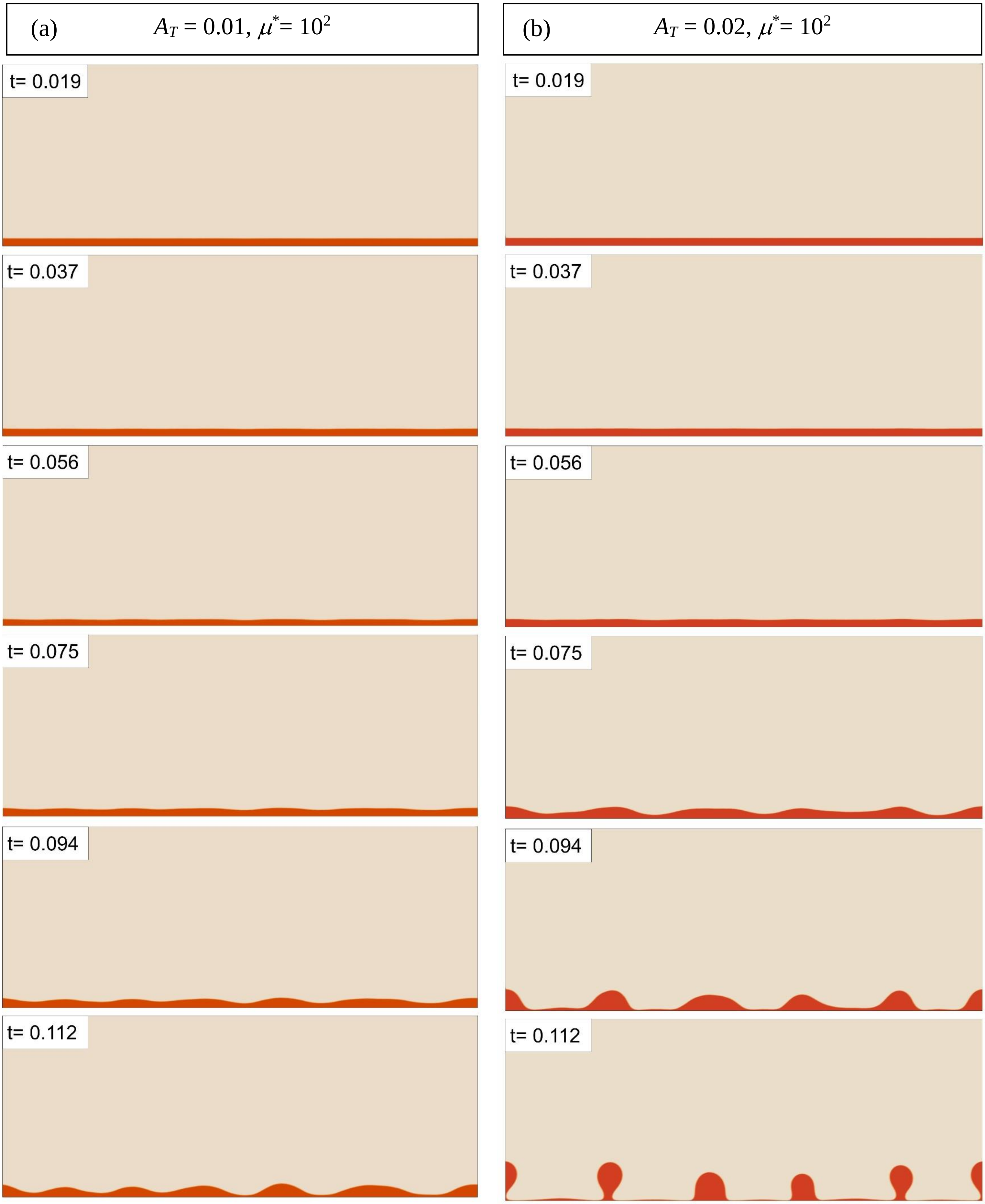

(a) $A_T = 0.01$, $\mu^* = 10^2$
(b) $A_T = 0.02$, $\mu^* = 10^2$
t= 0.019
t= 0.037
t= 0.056
t= 0.075
t= 0.094
t= 0.112

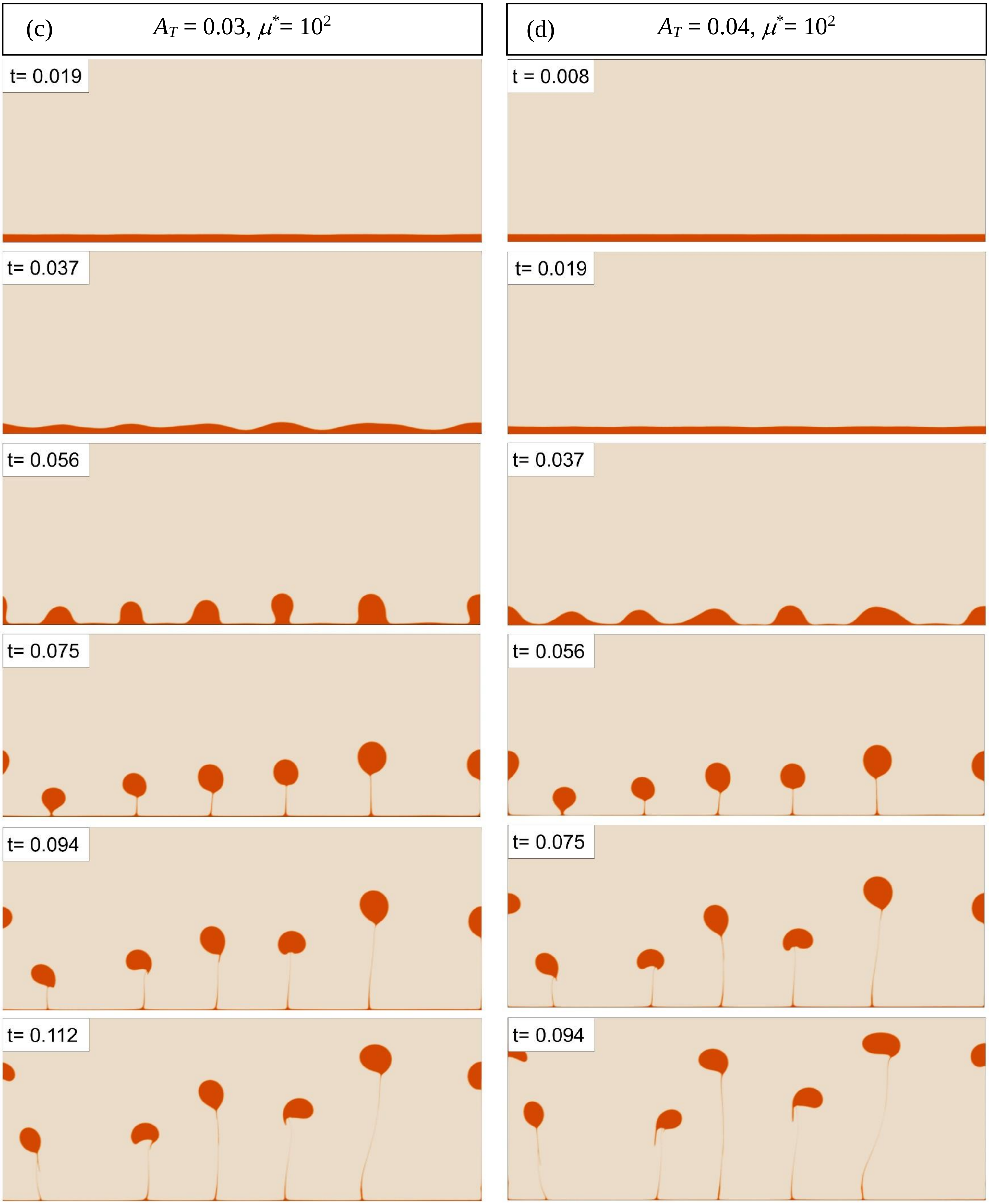
(c) $A_T = 0.03$, $\mu^* = 10^2$
t= 0.019
t= 0.037
t= 0.056
t= 0.075
t= 0.094
t= 0.112
(d) $A_T = 0.04$, $\mu^* = 10^2$
t = 0.008
t= 0.019
t= 0.037
t= 0.056
t= 0.075
t= 0.094

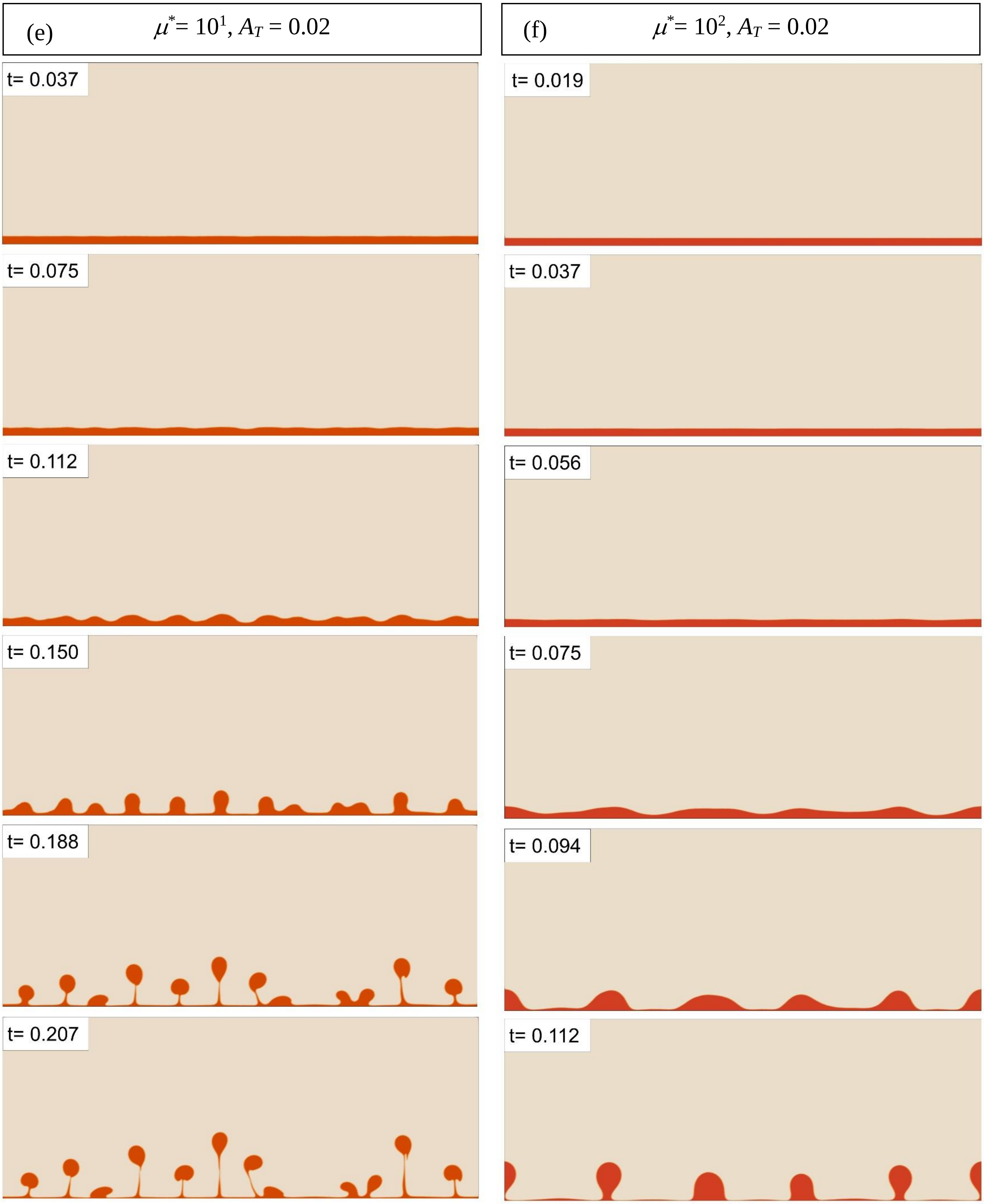

(e)
$\mu^* = 10^1, A_T = 0.02$
t= 0.037
t= 0.075
t= 0.112
t= 0.150
t= 0.188
t= 0.207
(f)
$\mu^* = 10^2, A_T = 0.02$
t= 0.019
t= 0.037
t= 0.056
t= 0.075
t= 0.094
t= 0.112

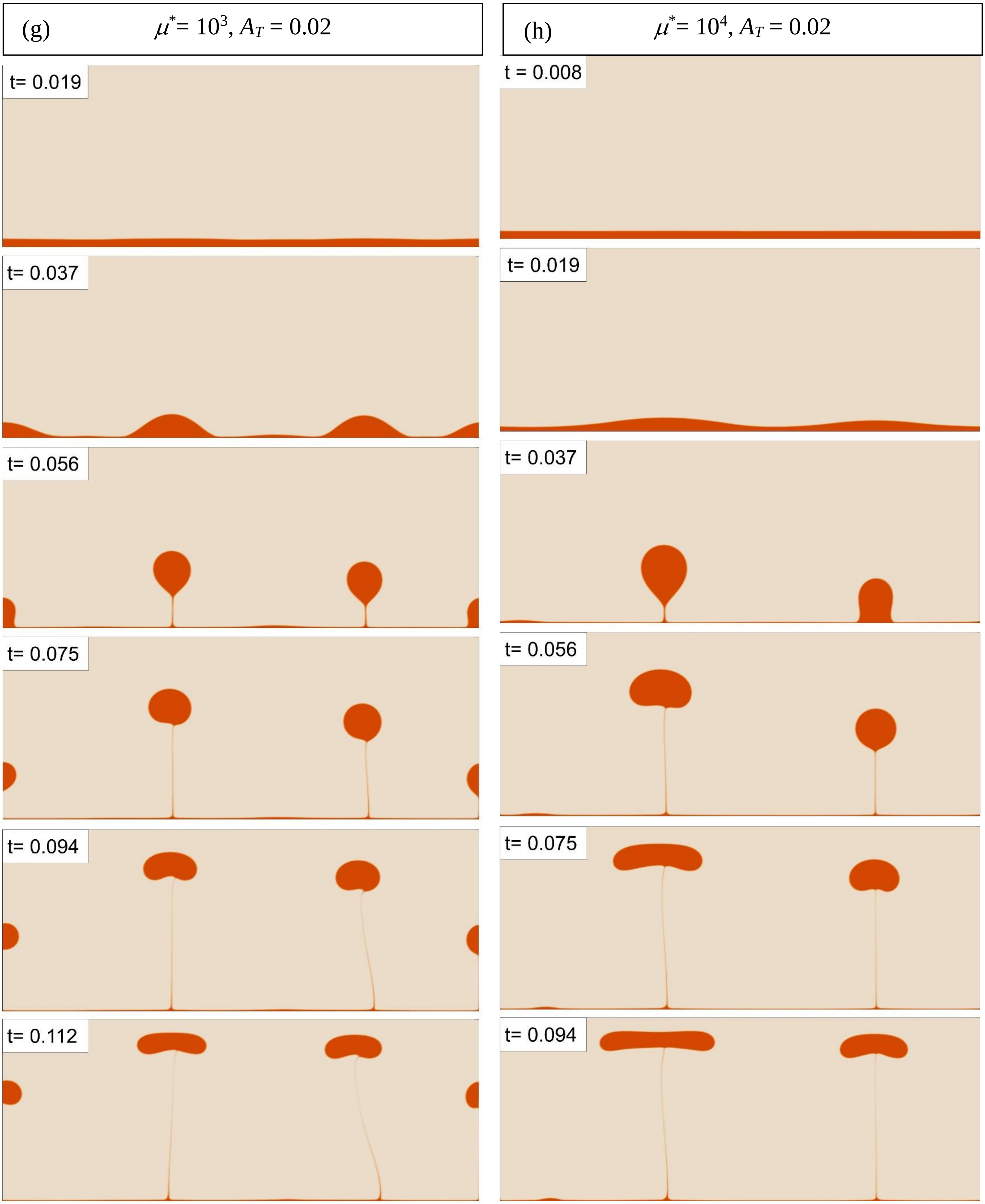
(g) $\mu^* = 10^3$, $A_T = 0.02$
(h) $\mu^* = 10^4$, $A_T = 0.02$
t= 0.019
t= 0.037
t= 0.056
t= 0.075
t= 0.094
t= 0.112
t = 0.008
t= 0.019
t= 0.037
t= 0.056
t= 0.075
t= 0.094

Figure S5: (a) – (h) Progressive development of Rayleigh-Taylor instabilities in CFD models with varying Atwood number (A_T) and viscosity ratio (μ^*).

S6: Model plume spacing

We performed sets of numerical experiments to study the plume spacing by varying the overburden to source-layer viscosity ratio, μ* and normalized source-layer thickness h_2. The graphical plot shown in Fig. S6a clearly show a nonlinear increase of the spacing with increasing μ*. The spacing also increases with the normalised source-layer thickness (Fig. S6b).

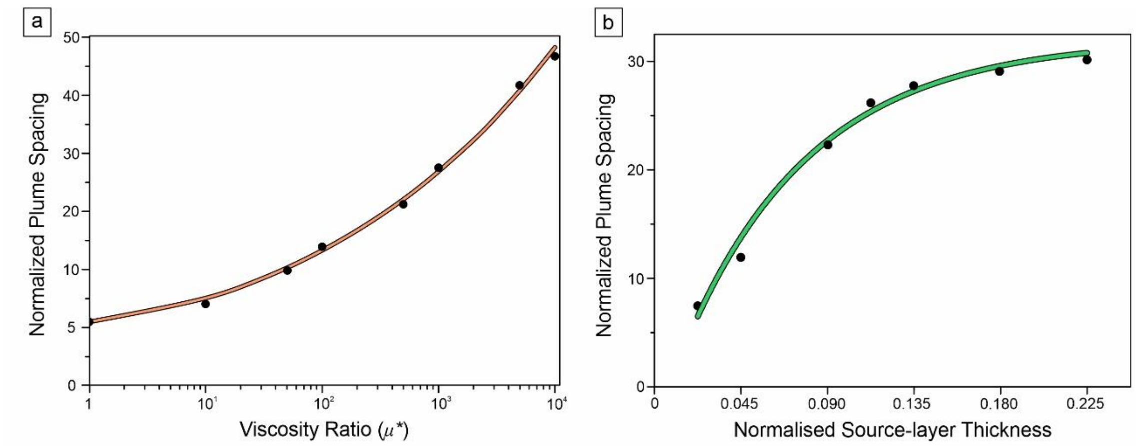

Figure S6: Normalized plume spacing as a function of (a) viscosity ratio (μ^*), and (b) normalised source layer thickness. The plume spacing is normalized by $h_2 = 0.045$

S7: Analytical Results

Using the dispersion relation (Eq. 36) from the linear stability analysis we performed numerical analyses of the growth rate, σ of instability for varying initial source-layer thickness, h_0 and different k_m versus k relations. The graphical plots indicate that the instability can grow at the fastest rate on a specific wavenumber (i.e., dominant wavelength). For extremely thin layers (low value of h_0), the long waves remain marginally stable or unstable (Fig. S7a). The short waves, in contrast, are always stabilized, primarily due to viscous effects of the thin-layer. Unlike the previous factors, increasing h_0 decreases the wavenumber corresponding to the most dominant mode that agrees well with the common observation that the wavelength of instabilities holds a positive correlation with layer thickness. For a given h_0 value, a switch over in the condition from $k_M = k$ to $k_M \ll k$ promotes the destabilizing state in the system (Fig. S7b, dashed lines) both in terms of increasing growth rate and wavenumber (i.e., reducing wavelength).

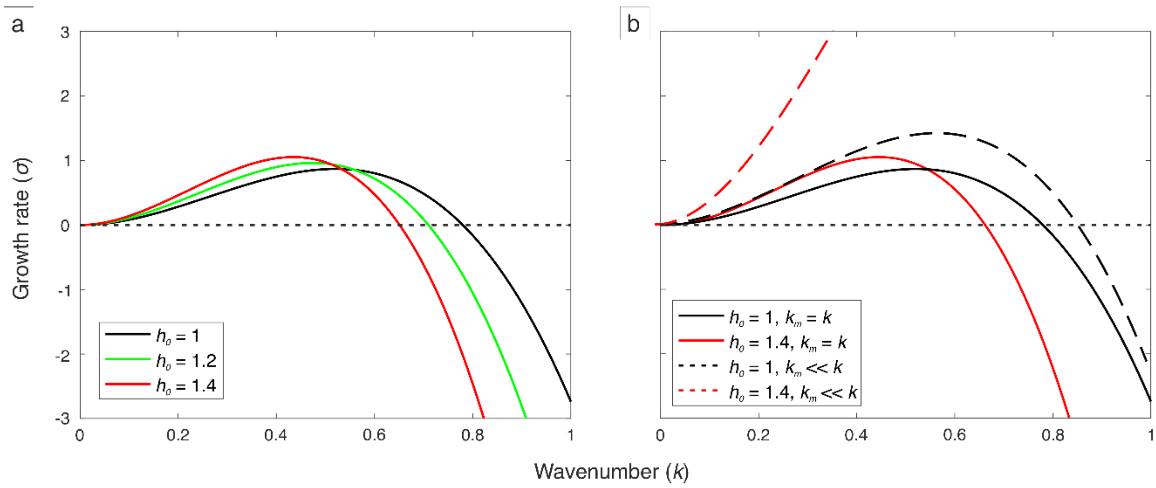

Figure S7: Growth rate σ versus wavenumber k plots for different values of initial source-layer thickness h_0 for (a) $k_m = k$, and (b) for $k_m \ll k$. The plots are based on Eq. 36 (main text).